





Electronic materials



Understanding the local structure of Eu³⁺- and Y³⁺-stabilized zirconia: insights from luminescence and X-ray absorption spectroscopic investigations

M. Eibl¹ , S. Shaw², D. Prieur¹ , A. Rossberg¹, M. C. Wilding³, C. Hennig¹ ,
K. Morris², J. Rothe⁴, T. Stumpf¹, and N. Huittinen^{1,*} 

¹Institute of Resource Ecology, Helmholtz-Zentrum Dresden-Rossendorf, Bautzner Landstraße 400, 01328 Dresden, Germany

²Research Centre for Radwaste Disposal and Williamson Research Centre, School of Earth, Atmospheric and Environmental Science, University of Manchester, Manchester M13 9PL, UK

³University of Manchester at Harwell, Diamond Light Source, Harwell Campus, Didcot OX1 0DE, UK

⁴Institute for Nuclear Waste Disposal, Karlsruhe Institute of Technology, Hermann-von-Helmholtz-Platz, 76344 Eggenstein-Leopoldshafen, Germany

Received: 16 March 2020

Accepted: 30 April 2020

Published online:

18 May 2020

© The Author(s) 2020

ABSTRACT

This study combines bulk structural and spectroscopic investigations of Eu³⁺- or Y³⁺/Eu³⁺ co-doped tetragonal and cubic zirconia polymorphs to gain an in-depth understanding of the solid solution formation process. Our bulk structural characterizations show that the dopant is homogeneously distributed in the ZrO₂ host structure resulting in an increase of the bulk symmetry with increasing dopant substitution (from 8 to 26 mol%). The local site symmetry around the Eu³⁺ dopant, however, determined with luminescence spectroscopy (TRLFS), remains low in all samples. Results obtained with X-ray pair distribution function and X-ray absorption spectroscopy show that the average coordination environment in the stabilized zirconia structures remains practically unchanged. Despite this very constant average dopant environment, site-selective TRLFS data show the presence of three nonequivalent Eu³⁺ environments in the ZrO₂ solid structures. These Eu³⁺ environments are assumed to arise from Eu³⁺ incorporation at superficial sites, which increase in abundance as the size of the crystallites decrease, and incorporation on two bulk sites differing in the location of the oxygen vacancies with respect to the dopant cation.

Address correspondence to E-mail: n.huittinen@hzdr.de

<https://doi.org/10.1007/s10853-020-04768-3>

 Springer

Introduction

Zirconia (ZrO_2) is a material with exceptional properties such as a very high melting point of 2715 °C and the capability of forming solid solutions with various isovalent and aliovalent cations [1]. The incorporation of under- or oversized cations leads to a phase transformation from the thermodynamically stable phase, i.e., the monoclinic phase under ambient conditions, to its high temperature polymorphs, the tetragonal or cubic structures, depending on the type and amount of dopant [2–4]. In case of isovalent substitution of Zr^{4+} , the mismatch of the ionic radii of the host versus dopant cation causes a distortion of the crystal lattice, leading to the aforementioned phase transition. When subvalent doping is performed, charge compensation takes place via the introduction of oxygen vacancies into the system. This is assumed to have a strong stabilizing effect on the *t*- and *c*- ZrO_2 phases [4, 5]. The incorporation of supervalent dopants is also feasible; however, less is known about these structures [3]. Due to this unique set of properties, the material can be tailored to meet the requirements of the targeted applications. The three most common stabilizers are ceria (CeO_2), yttria (Y_2O_3) and magnesia (MgO). CeO_2 -doped ZrO_2 is used in three-way catalysts of internal combustion engines [6]. Y_2O_3 -stabilized zirconia (YSZ) exhibits very good oxygen conducting properties, resulting from the oxygen vacancy formation in ZrO_2 . At the same time, YSZ is acting as an electrical insulator. In combination with the very high temperature stability, this makes it an ideal electrode material in the field of solid oxide fuel cells (SOFCs). Besides the use of YSZ as cathode material due to the high oxygen mobility [7–9], it also finds application as basis for the anode material in SOFCs, where a metallic anode material is deposited on the YSZ [10–12]. YSZ is further used as sensor material for reducing gases, such as CO , H_2 and hydrocarbons but also for H_2S and NO_x [13]. MgO -stabilized ZrO_2 is an important construction material due its exceptional strength and fracture toughness. The fracture toughness rests upon the martensitic transformation of metastable *t*- ZrO_2 to *m*- ZrO_2 , which is accompanied by a volumetric expansion. This expansion resulting from the diffusionless transformation, induced by the stress field around a crack in a ZrO_2 ceramic material, leads to local compressive stress which counterweighs the driving

force of the crack propagation [1, 14–16]. Besides these three very commonly studied materials, applications for various other stabilizing cations can be found. Ti^{4+} , Al^{3+} or K^+ -stabilized ZrO_2 can be used as catalysts in the biofuel production [17]. Lanthanide-stabilized zirconia finds usage, especially in the field of optoelectronics [18–29]. Further research of lanthanide-doped ZrO_2 has been performed in the field of oxygen ion conductors [30], basic material properties [31–33], as well as in fundamental research. Zirconia is also studied in nuclear research in relation to the transmutation of actinides (An) [34–37], and the production of inert matrix fuels [38, 39]. Furthermore, ZrO_2 is an important solid phase at several stages of the nuclear fuel cycle. It occurs as a corrosion product at the fuel rod cladding surface where it may come into contact with dissolved radionuclides in repositories for nuclear waste storage, and it has been considered a potential host matrix for the immobilization of high-level radioactive waste streams containing especially the transuranium elements (TRUs) Pu, Am and Cm [40–42]. The most stable oxidation state of the latter two TRUs is +3, while Pu^{3+} can be stabilized under anoxic, mildly reducing conditions. For applications as nuclear materials, the crystalline host structure must be flexible enough to accommodate the rather large actinide cations. Further, structural properties such as a large overall grain size and low porosity, which reduce the reactive surface area and subsequently increase their corrosion resistance in contact with water, are important.

Due to the large amount of applications for ZrO_2 doped with trivalent rare earth elements (REE), special interest exists in the structural properties of these solid phases. The formation of oxygen vacancies in the lattice as a result of REE^{3+} incorporation leads to a deviation between the long-range order in the bulk and the short-range order of the local structure. Despite the increase in the bulk symmetry from *m*- to *t*- to *c*- ZrO_2 with increasing doping fractions, the local symmetry is heavily distorted in these stabilized *t*- and *c*- ZrO_2 phases. A change in the coordination number from 8 to 7 occurs, especially for the Zr^{4+} but also for the trivalent dopant depending on the overall concentration of oxygen vacancies in the crystal structure [4]. The reduction in the Zr–O coordination number is assumed to result in the stabilization of the high-temperature phases, due to a reduction of the stress around the small Zr^{4+} cation. In addition,

distortion of the crystal structure takes place due to the size mismatch between the small Zr^{4+} and the much larger REE^{3+} cations.

The structural properties of zirconia solid solutions have been investigated in numerous studies using various experimental and computational methods. Several extended X-ray absorption fine structure (EXAFS) studies of doped zirconia phases have been conducted with various trivalent dopants such as Fe^{3+} , Ga^{3+} , Ge^{3+} , Nb^{3+} , Ce^{3+} , Gd^{3+} [4, 43], Er^{3+} [44] and Am^{3+} [36]. YSZ has received especially large attention in this field [45–49]. The EXAFS studies have shown that the direct coordination environment around the dopant stays very constant, independent of the ZrO_2 crystal phase. This has partly been explained by the location of the oxygen vacancies in the crystal structure and their preference for the Zr^{4+} cation rather than the dopant cation [36, 45]. Laser-induced lanthanide luminescence spectroscopy, especially of Eu^{3+} , has further been employed to study the local structure of zirconia solid solutions [1, 21, 30–32, 50–55]. Here, differing luminescence behavior is observed for m - ZrO_2 as compared to the high-temperature polymorphs (t - and c - ZrO_2). However, no significant change in the luminescence of Eu^{3+} doped t - ZrO_2 and c - ZrO_2 can be observed, especially when using the classical nonselective excitation method, which results in co-excitation all Eu^{3+} environments in the crystal structure. When using site-selective excitation of the ${}^5D_0 \leftarrow {}^7F_0$ or the ${}^5D_1 \leftarrow {}^7F_0$ transition, multiple Eu^{3+} species have been observed in several studies [30–32, 50–52, 55]. However, contradicting conclusions have been drawn on the nature of the individual species, and their assignment to specific luminescence emission spectra. Various computational studies have been performed to investigate structural properties of doped zirconia phases [56–61]. Special interest in experimental and computational studies has been devoted to the oxygen diffusion in YSZ [62–65]. It was found that the doping fraction and the location of oxygen vacancies in the lattice are crucial for the oxygen mobility in these phases [58, 62].

Despite the existing knowledge of t - and c - ZrO_2 phases stabilized with trivalent cations, knowledge gaps still exist regarding the relationship between the bulk structure and order/disorder phenomena occurring around the dopant cation. To our knowledge, no direct comparison of changes occurring in the dopant (Ln^{3+}) versus Zr^{4+} environments has been

attempted, which could provide a deeper insight into how similar or dissimilar structural changes around the host and dopant cations are for various dopant concentrations and how they influence the overall symmetry of the bulk structure in comparison with order/disorder phenomena on the dopant level.

Thus, in the present work, we report on first combined luminescence spectroscopic (TRLFS) and EXAFS investigations of Eu^{3+} or Y^{3+}/Eu^{3+} co-doped tetragonal and cubic zirconia polymorphs. Powder X-ray diffraction (PXRD) has been used to study the bulk behavior of doped zirconia phases in dependence of the doping percentage. Scanning electron microscopy (SEM) and transmission electron microscopy (TEM) were employed as imaging method for macroscopic investigations. Site-selective Eu^{3+} TRLFS at 10 K was used to study the local dopant environment independently from the bulk. Additionally, EXAFS investigations at the yttrium and zirconium K-edges were performed on Y^{3+}/Eu^{3+} co-doped zirconia samples for complementary information on the local structure of the dopant and the host cations. To bridge the gap between the bulk structural and dopant-specific investigations, additional X-ray pair distribution function (XPDF) analyses were conducted for Eu^{3+} doped zirconia samples. XPDF is a complementary method to study local structures and disorder phenomena in crystalline as well as amorphous materials, capable of providing information of the average, periodic structure of a material as well as potential local deviations from this average structure. While many studies can be found where the PDFs of zirconia systems were obtained based on computational approaches [63, 66, 67], the availability of PDFs based on experimental data [i.e., X-ray diffraction (XPDF) or neutron diffraction (NPDF)] is rather limited. To the best of our knowledge, only one study can be found where the XPDF of a monoclinic zirconia sample is presented [68]. Therefore, we report on the first XPDF studies on stabilized ZrO_2 polymorphs in the present work.

Experimental

Sample preparation

Two separate solid solution rows were produced for the various spectroscopic investigations conducted in

the present work. Eu^{3+} doped ZrO_2 samples with europium concentrations ranging from 8 to 24 mol% were synthesized for luminescence spectroscopic investigations. To avoid luminescence energy transfer between closely located luminescence centers in the samples and due to a better accessibility of the Y K-edge in comparison to the low-energy L edges of Eu, $\text{Y}^{3+}/\text{Eu}^{3+}$ co-doped zirconia samples with an overall dopant concentration of 16–26 mol% were synthesized for combined TRLFS and EXAFS investigations. XPDF investigations were conducted for Eu^{3+} doped samples ranging from 16 to 24 mol% Eu^{3+} . In a typical ZrO_2 synthesis, 400 mg of $\text{ZrOCl}_2 \cdot 8\text{H}_2\text{O}$ (> 99.5%, Sigma-Aldrich) was dissolved in 1 mL of 0.01 M HCl (Carl Roth, ROTIPURAN p.a.). To reach a dopant level of 8–24 mol% Eu^{3+} in the final product, the acidic Zr^{4+} -containing solution was mixed with an adequate amount of 0.1 M Eu^{3+} solution, prepared from $\text{EuCl}_3 \cdot 6\text{H}_2\text{O}$ (99.9% purr., Sigma-Aldrich). For the synthesis of Y^{3+} and Eu^{3+} co-doped samples with a constant Eu^{3+} content of 0.5 mol%, and varying Y^{3+} concentrations, to reach an overall dopant level of 16–26 mol% in the final ZrO_2 material, the acidic Zr^{4+} -containing solution was mixed with 0.1 M Y^{3+} solution ($\text{YCl}_3 \cdot 6\text{H}_2\text{O}$, 99.99% purr., Sigma-Aldrich), containing a small amount of Eu^{3+} . The acidic metal ion solution (Zr^{4+} , $\text{Eu}^{3+}/\text{Y}^{3+}$) was added dropwise to an alkaline solution of NaCl (pH \sim 12) with a concentration of 0.5 M. The pH was constantly monitored during addition of the acidic precursor solution and readjusted to pH 12 with 2 M NaOH solution when necessary. The exact doping fractions were determined by ICP-MS of the acid solutions and resulted in 7.8 mol%, 9.6 mol%, 11.3 mol%, 13.0 mol%, 16.1 mol%, 19.0 mol% and 24.4% for the Eu^{3+} rows and 15.6 mol%, 18.4 mol%, 23.5 mol% and 26.4 mol% in the case of Y^{3+} doping. In the following text, sample compositions will be rounded off to whole numbers. Furthermore, the individual samples will be referred to by dominating crystal phase as determined by Rietveld analysis, i.e., *t*- ZrO_2 for a sample where the largest fraction is tetragonal. After the addition of the whole precursor solution, the suspension was kept at 80 °C for 20 h to allow for complete precipitation. Thereafter, the suspension was separated by means of centrifugation and washed twice with 25 mL of Milli-Q water. The residual was dried at 80 °C for 20 h and then transferred into an alumina crucible for calcination at

1000 °C for 5 h with a heating ramp of 16 K/min. After cooling, the resulting doped ZrO_2 solid was mortared into a fine powder.

Bulk characterization methods

The phase composition of the synthetic doped zirconia phases was analyzed with PXRD. The PXRD studies were performed at the Rossendorf beamline (ROBL) at the European synchrotron research facility (ESRF) in Grenoble, France. The measurement setup has a rotating capillary sample holder and a Pilatus 3×2 M detector. The X-ray wavelength was set to 0.73804 Å. Each sample was measured for a total of 10 min.

SEM and TEM were combined to investigate both particle morphology and size and to confirm a homogeneous distribution of the dopant in ZrO_2 . The SEM images were obtained on a FEI Quanta 650 with samples either as powder or from suspension on a stub holder. TEM measurements were performed on a FEI Tecnai F30 where the samples were applied from suspension on a TEM grid.

High-energy X-ray diffraction data for X-ray pair distribution function (XPDF) analysis were collected at I15-1, Diamond Light Source using X-rays with incident energy of 76.7 keV ($\lambda = 0.161669$ Å). The experiment was performed in transmission geometry with samples loaded into borosilicate glass capillaries. The scattered X-rays are typically collected on a scintillation detector (Perkin Elmer XRD 43434 CT), and the two-dimensional scattering patterns were reduced to one-dimensional patterns by integrating over the detector pixels. Sample–detector distance and parameters such as polarization and detector tilt are determined by calibrating with a crystalline standard. The total structure factor $[S(Q)]$ is obtained by using diffraction data for the samples and an empty capillary, normalizing to the X-ray form factor with corrections for sample absorption and Compton scattering, in this case using the program PDFgetX2 [69]. The short wavelengths and access to high values of scattering vector result in high real-space resolution and transforms of the $S(Q)$ to pair distribution functions (PDFs) that were then used in combination with the PDF analysis programs (PDFGui [70]) to fit structures based on crystallographic input files for the cubic zirconia samples [71].

TRLFS studies of Eu^{3+} incorporated into zirconia

For the site-selective TRLFS measurements, a pulsed dye laser (NarrowScan, Radiant Dyes) with Rhodamine 6G dye, coupled to a Nd:YAG (Continuum, Surelite) pump laser was used. The excitation wavelength was varied between 570 and 585 nm, and the pulse energy was between 4 and 5 mJ. These experiments were conducted at temperatures below 10 K, using a He-refrigerated cryostat (Janis and Sumitomo, SHI cryogenics group). The Eu^{3+} luminescence emission spectra were recorded between 570 and 650 nm, 1 μs after the exciting laser pulse. Luminescence emission was detected by an optical multi-channel analyzer (Shamrock 303i) with 300, 600 or 1200 lines/mm grating and an ICCD Camera (iStar, Andor). Lifetime measurements were performed by monitoring the luminescence emissions with 5 μs and 500 μs time delay steps between the laser pulse and the camera gating. The obtained lifetimes can be correlated with the number of water molecules in the first hydration sphere of the Eu^{3+} cation with the semiempirical *Horrocks* equation [72] (Eq. (1)). For a fully incorporated metal cation, coordinating water molecules should be completely absent, resulting in long luminescence lifetimes above 1.7 ms.

$$N_{\text{H}_2\text{O}} = \frac{1.07}{\tau_{\text{Eu}^{3+}}[\text{ms}]} - 0.62 \quad (1)$$

EXAFS studies of the local environment of Zr^{4+} and Y^{3+} in stabilized zirconia

Yttrium doped zirconia was prepared following the synthesis method described above. The samples were diluted with α -cellulose powder (Sigma-Aldrich) to an analyte concentration of 1 wt% and pressed into a pellet with a handheld press. The pellets were placed in a polyethylene confinement for the EXAFS measurements. The measurements were performed at the INE-Beamline [73, 74] at the KIT synchrotron source, Karlsruhe, Germany, at the Zr-K- and Y-K-edge at room temperature in transmission mode. The storage ring operating conditions were 2.5 GeV and 80–120 mA. A Ge(422) double-crystal monochromator coupled with collimating and focusing Rh-coated mirrors was used. XAFS spectra at the Zr K- (17.998 keV) and at the Y K-edge (17.038 keV) were recorded in transmission mode using Ar-filled

ionization chambers at ambient pressure. For energy calibration, XAFS spectra of Zr and Y metal foils were recorded simultaneously. The data were analyzed using the WinXAS software [75]. The Fourier transformation of the experimental EXAFS spectra was performed using a Hanning window over the k range of 2 and 10.5 \AA . Phases and amplitudes of the interatomic scattering paths were calculated using FEFF8.20 [76]. A spherical cluster of atoms with the radius of 5.6 \AA was made using the fluorite-type structure (space group $\text{Fm}\bar{3}\text{m}$ was used in the FEFF calculation). An amplitude reduction factor (S_0^2) of 1.0 was used, and the number of independent variables was 16 in all fits. Fitting was performed in R-space in a range from 1.4 to 4.5 \AA .

Results

Bulk structural investigations of zirconia solid solutions

Electron microscopy imaging

SEM images of the polished samples were taken and combined with energy-dispersive X-ray spectroscopy (EDX) to investigate the distribution of the dopant ion within the zirconia matrix. Based on the results of the elemental mapping, a homogeneous distribution of the dopant within the zirconia matrix could be confirmed (see Figure S1 in the supporting information, SI).

The TEM images of nonstabilized (Fig. 1, left) and stabilized (Fig. 1, middle and right) zirconia show agglomerates of smaller particles with a heterogeneous morphology. The largest particles are obtained for the nondoped (monoclinic) solid phase. The stabilized structures with varying Eu^{3+} content are composed of smaller particles which seem to decrease in size when going from lower (middle figure) to higher (right figure) Eu^{3+} doping. Due to the strong agglomeration tendency of the particles, a clear determination of the crystallite size could not be made based on the TEM images.

The electron diffraction image of the $m\text{-ZrO}_2$ sample without dopant (Fig. 1, bottom, left) shows a very ordered reciprocal crystal lattice of the monoclinic structure. This indicates that only a single or very few crystallites are within the focus of the electron beam. At higher doping percentages, a more diffraction

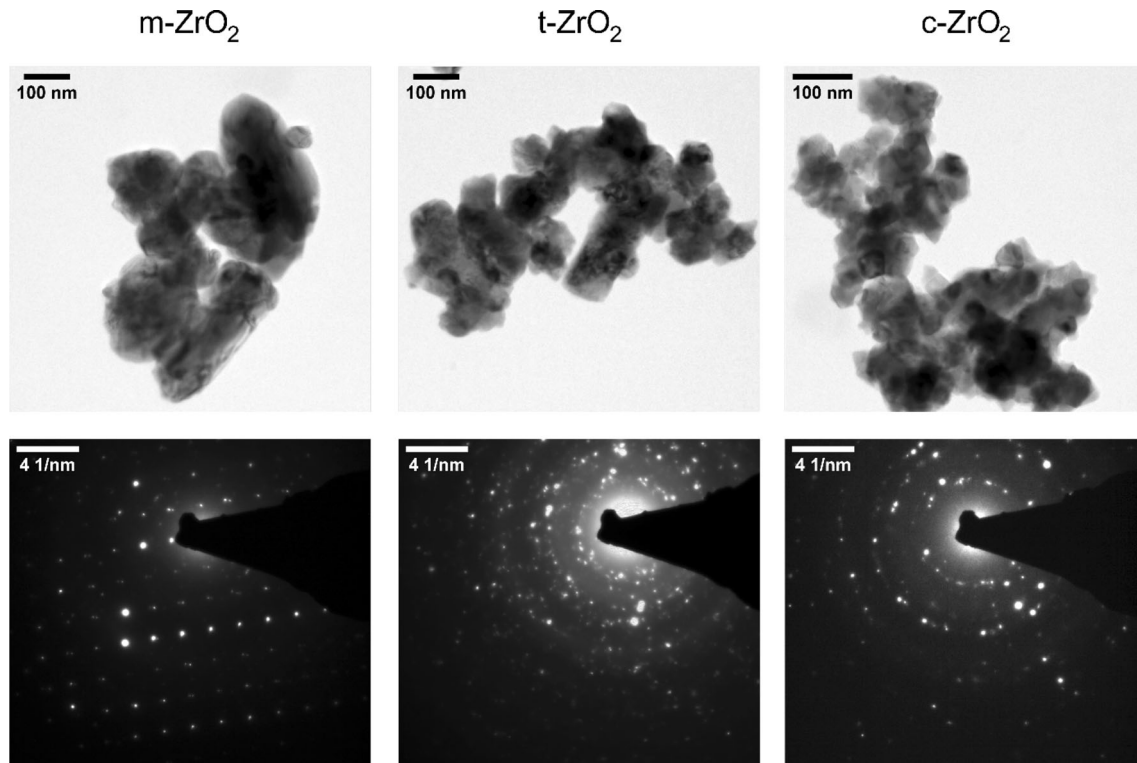


Figure 1 TEM images (top) and electron diffraction images (bottom) of nonstabilized m -ZrO₂ (left), t -ZrO₂ doped with 8 mol% Eu³⁺ (middle) and c -ZrO₂ doped with 19 mol% Eu³⁺ (right).

ring-like image becomes visible. Therefore, it can be deduced that a larger quantity of crystallites are within the electron beam spot and further that the crystallite size is likely to be smaller in the stabilized phases than in the monoclinic one.

Influence of Y³⁺/Eu³⁺ doping on the bulk structure of zirconia

Examples for observed diffraction pattern of pristine m -ZrO₂ and Eu³⁺-stabilized t - and c -ZrO₂ are presented in Fig. 2, left. Two different stabilizer cations have been used in the various studies, i.e., Eu³⁺ and Y³⁺. Using Rietveld refinement, the phase percentages of the individual m -, t - and c -phases were determined from the diffraction pattern. The combined results for Eu³⁺ doped and Y³⁺/Eu³⁺ co-doped solids are presented in Fig. 2, right. Both sample rows differing in the stabilizing ion used in the synthesis differ only within margin of error regarding their phase composition. Therefore, it can be assumed that Eu³⁺ doped and Y³⁺/Eu³⁺ co-doped ZrO₂ samples with the same overall dopant concentration are directly comparable.

In the phase diagram of Y₂O₃-ZrO₂ derived by Fabrichnaya and Aldinger [77], at a temperature below 1040 °C and a Y³⁺ mole fraction of below about 24%, a miscibility gap between the monoclinic and the cubic phases exists. Therefore, all samples with a phase composition ranging from 0 to 24 mol% should segregate in pristine m -ZrO₂- and Y³⁺ doped c -ZrO₂. However, the extraordinarily slow cation mobility in zirconia hinders this phase segregation. In fact, Chevalier et al. [78] have estimated that for grains of 500 nm size, the complete diffusion of the Y-cations at 1000 °C would take more than 31 years. Therefore, it can be assumed that no or very little cation diffusion takes place over the 5 h calcination time in the synthesis performed here. As a result, the phase diagram does not yield information of the expected phase compositions.

In studies performed by Scott [79], where sintered specimens had not been kept at high temperatures until equilibrium and had been quenched to room temperature rapidly, a gradient transition for Y³⁺ doped zirconia from monoclinic (0–5 mol%) to tetragonal (4–13 mol%) to cubic ZrO₂ (from 12 mol%) was observed.

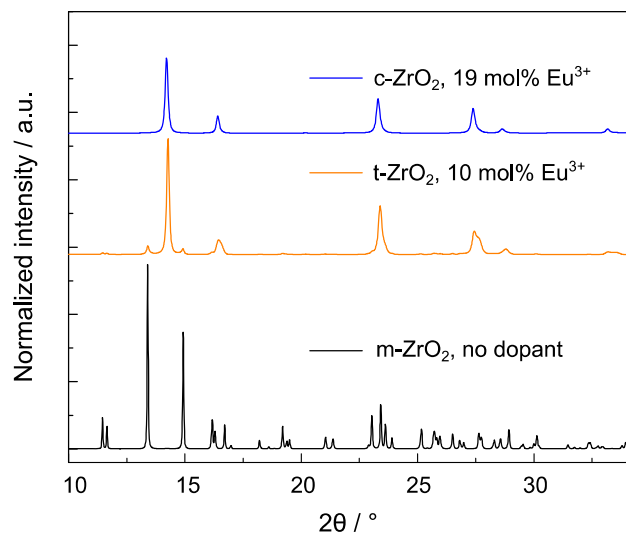
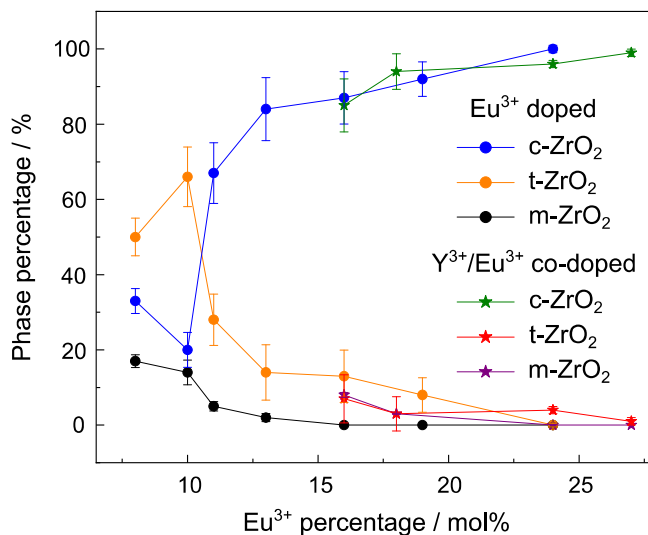


Figure 2 Diffractogram of m -ZrO₂ with no dopant (black), t -ZrO₂ with 10 mol% Eu³⁺ doping (orange) and c -ZrO₂ with 19 mol% doping (blue) (left). Comparison of results of Rietveld

This is in agreement with our studies, where a comparable, rather continuous transformation from a mixed-phase system of m -, t - and c -ZrO₂ to a purely cubic phase can be seen. The Eu³⁺ doped samples show a three-phase regime for dopant percentages below 16 mol%. At higher doping fractions, the nonstabilized monoclinic phase disappears. The maximum fraction of the tetragonal phase can be seen for 10 mol% Eu³⁺ where it reaches a percentage of about 70%. This is followed by a steep decrease of t -ZrO₂ and a steep increase of the cubic phase, where the latter one is the dominating polymorph from about 16 mol% doping onward. It increases to 100% for the highest Eu³⁺ doping percentage. The diffraction patterns of both the Eu³⁺ doped and Y³⁺/Eu³⁺ co-doped samples do not show any peaks resulting from the formation of secondary phases such as pyrochlore. Pyrochlores of the type Eu₂Zr₂O₇ have been observed to form at doping fractions typically larger than 30 mol% [80, 81]. The smaller cation radius of Y³⁺ in Y₂Zr₂O₇ is unsuitable for the formation of pyrochlore structures [82]; therefore, a fluorite-type bulk structure can be found even in stoichiometric mixtures. Nevertheless, it has been observed that ordered pyrochlore micro domains can exist in these phases [83]. Due to the absence of visible diffuse scattering in the diffractograms, a large abundance of such micro-domains is not expected.

For the Y³⁺/Eu³⁺ co-doped samples, the trend is very similar; however, the monoclinic phase persists



refinement for purely Eu³⁺ doped samples in the dopant range from 8 to 24 mol% (closed dots) and Y³⁺/Eu³⁺ co-doped samples in the range from 16 to 26 mol% (asterisks) (right).

as a very minor amount up to concentrations of 18 mol% after which an almost pure cubic phase can be observed. Its percentage increases to 100% for the highest doping percentage, i.e., 26 mol%. Between 16 mol% and 24 mol%, a small amount of the tetragonal phase can be observed.

It should be noted that the phase percentages inherit a rather large error margin, especially in the region of intermediate M³⁺ doping, where all three structures coexist. This error from the Rietveld refinement is caused by the very large overlap of the diffraction patterns of the stabilized tetragonal and cubic phase, as visualized in Figure S2, for selected mixed-phase samples. Here, it is evident that even peaks of higher diffraction order, such as the cubic and the tetragonal (004) peaks, show a strong overlap rather than distinctive peaks for each phase. Furthermore, the samples show a considerable amount of peak broadening, indicative of small crystallites, which hinders clear phase quantification.

The lattice parameters derived from the diffractograms of the Eu³⁺ doped tetragonal phase (Fig. 3, left) show an increasing behavior with increasing Eu³⁺ doping in the parameters a and b , and decreasing in parameter c . In Fig. 3, right, one can see that also the lattice parameters of the cubic phase increase with increasing doping. In accordance with Vegard's law, a linear slope of the lattice parameters is seen in the region where the cubic phase is the dominating phase (85% and above). A linear trend of

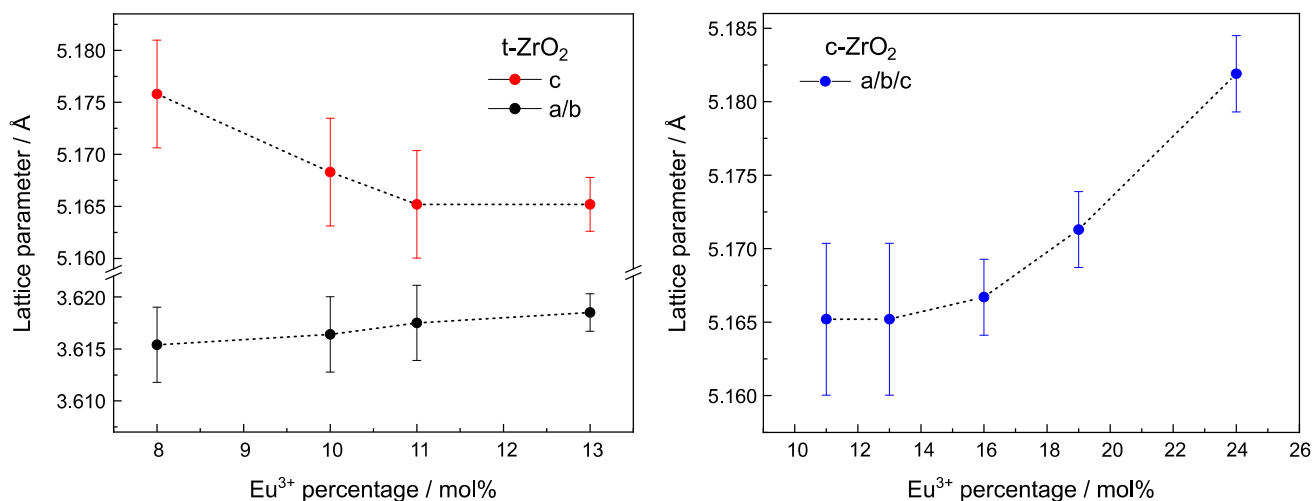


Figure 3 Comparison of the lattice parameters $a (= b)$ and c of the tetragonal zirconia in dependence of the europium fraction from 10 to 13 mol% (left) and lattice parameters of the cubic stabilized zirconia from 11 to 24 mol% Eu^{3+} (right).

the lattice parameters in the pure cubic phase region implies that no secondary phases are present in the samples. At lower doping fractions, the mixture of phases is causing the observed nonlinear behavior. The aforementioned strong overlap of the diffraction peaks also causes a rather large error associated with the lattice parameters.

Thus, to gain further confidence in the bulk structural parameters, collected XPDF data were analyzed and compared with the results obtained by PXRD. The PDFs of all sample compositions from 16 to 24 mol% Eu^{3+} can be well described using only a fluorite-type cubic zirconia crystal structure. This is visualized in Fig. 4. The experimental total scattering function $S(Q)$ does not show a noteworthy change in the diffuse scattering component in this doping series (see Figure S3). This implies that no systematic change of the deviation from the average crystal structure takes place. The lattice parameters extracted from the XPDF data are compiled in Table S1 together with the results obtained from the refinement of our PXRD data. In general, a very good agreement between the two methods can be discerned. Slightly smaller lattice parameters (between 0.004 and 0.011 Å) are obtained with the XPDF method; however, the trend of increasing lattice parameters with increasing Eu^{3+} concentration is evident, corroborating the PXRD results discussed previously. In addition to the bulk structural data, interatomic distances were obtained from the XPDF fits. These are compiled in Table S2 and discussed in Sect. “EXAFS and

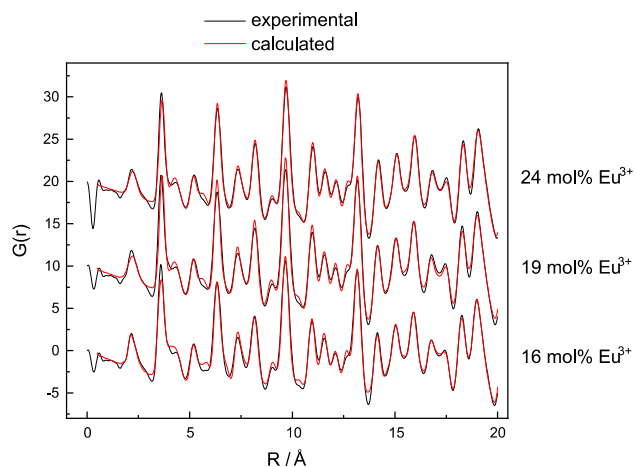


Figure 4 Comparison of experimental XPDF data to the fits generated from the crystal structure of cubic zirconia [71] for samples with 16–24 mol% Eu^{3+} . An offset is applied to the data as a visualization help.

XPDF studies of the local structure of M^{3+} doped zirconia”

Finally, the peak broadening in the diffraction pattern can have different origins. The increasing amount of the highly oversized dopant cation may introduce an increasing disorder of the bulk structure, resulting in the observed broadening of the diffraction peaks [84]. Generally, however, the largest contribution to peak broadening in powder diffraction is caused by small crystallite sizes below 100 nm, reducing the degree of long-range order. Here, the crystallite sizes were calculated using the Scherrer equation [85] and are presented in Table 1 together

Table 1 Summary of the main diffraction peak position and the resulting crystallite size derived from Scherrer equation ($K = 1$) for samples of Eu^{3+} doping of 8–24 mol% and for $\text{Y}^{3+}/\text{Eu}^{3+}$ co-doped zirconia with doping fractions of 18–26 mol%

Sample	Diffraction peak position/ $^{\circ} 2\theta$	FWHM*/ $^{\circ} 2\theta$	Crystallite size/nm
<i>t</i> -ZrO ₂ , 8 mol% Eu^{3+}	30.091 ± 0.005	0.269 ± 0.01	34 ± 1
<i>t</i> -ZrO ₂ , 10 mol% Eu^{3+}	30.091 ± 0.005	0.269 ± 0.01	34 ± 1
<i>t/c</i> -ZrO ₂ , 11 mol% Eu^{3+}	30.094 ± 0.005	0.290 ± 0.01	31 ± 1
<i>t/c</i> -ZrO ₂ , 13 mol% Eu^{3+}	30.071 ± 0.005	0.284 ± 0.01	32 ± 1
<i>c</i> -ZrO ₂ , 16 mol% Eu^{3+}	30.065 ± 0.005	0.300 ± 0.01	31 ± 1
<i>c</i> -ZrO ₂ , 19 mol% Eu^{3+}	30.025 ± 0.005	0.340 ± 0.01	27 ± 1
<i>c</i> -ZrO ₂ , 24 mol% Eu^{3+}	29.984 ± 0.005	0.433 ± 0.01	21 ± 1
<i>c</i> -ZrO ₂ , 16 mol% $\text{Y}^{3+}/\text{Eu}^{3+}$	30.083 ± 0.005	0.103 ± 0.01	88 ± 1
<i>c</i> -ZrO ₂ , 18 mol% $\text{Y}^{3+}/\text{Eu}^{3+}$	30.097 ± 0.005	0.106 ± 0.01	86 ± 1
<i>c</i> -ZrO ₂ , 24 mol% $\text{Y}^{3+}/\text{Eu}^{3+}$	29.992 ± 0.005	0.136 ± 0.01	67 ± 1
<i>c</i> -ZrO ₂ , 26 mol% $\text{Y}^{3+}/\text{Eu}^{3+}$	29.984 ± 0.005	0.144 ± 0.01	63 ± 1

*FWHM is corrected to subtract peak broadening from the setup via a Si reference sample

with the diffraction peak positions and the peak widths (FWHM).

As evident from Table 1, the $\text{Y}^{3+}/\text{Eu}^{3+}$ co-doped samples show narrower diffraction peaks indicative of larger crystallites. In both the Eu^{3+} doped and the $\text{Y}^{3+}/\text{Eu}^{3+}$ co-doped series, diffraction shows a decreasing crystallite size with increasing overall concentration of the dopant. This is supported by the microscopic investigations where a decreasing size of crystallites was observed with increasing doping (Fig. 1). However, a stronger distortion effect in the purely Eu^{3+} doped samples is likely to influence the diffraction peak widths as well to some extent, because of the slightly larger ionic radius of Eu^{3+} as compared to Y^{3+} . This could be a reason for the overall smaller crystallite size in the Eu^{3+} doping series.

Investigations of the local structure of M^{3+} stabilized zirconia

Eu³⁺ TRIFS investigation of the dopants local structure

To gain insight into the incorporation of Eu^{3+} in zirconia, such as the potential presence of multiple non-equivalent Eu^{3+} environments in the stabilized solid phases, site-selective TRIFS investigations at $T < 10$ K were performed.

Excitation spectra Figure 5, left, shows the excitation spectra of the $^5\text{D}_0 \leftarrow ^7\text{F}_0$ transition for Eu^{3+} doped ZrO₂ in the dopant concentration range where the main tetragonal phase transforms to the cubic zirconia phase.

For the compositions of intermediate doping (11–16 mol% Eu^{3+}), one broad excitation peak (FWHM ~ 1.9 nm) at a constant peak position of approximately 579.5 nm is observed. This is in contrast to Eu^{3+} incorporation in other crystalline phases, where the incorporation on a crystallographic host lattice site has been observed to yield very narrow excitation peaks (FWHM < 0.1 nm) in the highly ordered, crystalline environments [86, 87]. The inhomogeneous peak broadening of the $^5\text{D}_0 \leftarrow ^7\text{F}_0$ excitation peak observed here indicates that the environment of Eu^{3+} in the host is not very well defined but that the excitation peak consists of a multitude of species with slightly differing environments, which results in slightly different excitation energies [88]. This behavior has been observed before for Eu^{3+} doped zirconia [21, 32], as well as other doped phases such as tungstates, molybdates [87], pyrochlores [50] and several glasses [89, 90].

Furthermore, the change in the Eu–O bond length due to an increasing size of the crystal lattice (derived from extracted lattice parameters) has been shown to result in a very systematic blueshift of the Eu-excitation peak due to the weaker ligand field exerted on the Eu^{3+} cation by the coordinating oxygen ligands [86, 87]. In the present study, an increase in the lattice parameters was observed with PXRD and XPDF with increasing doping percentage (Fig. 3 and Table S1). Therefore, a blueshift of the excitation peaks would be expected in analogy with the aforementioned studies, due to an increasing Eu–O distance in the host phases. Instead, the excitation peak remains constant until 16 mol%. At very high doping, a blueshift of 0.2 and 0.4 nm is attained for the two highest Eu^{3+} dopant concentrations of 19 and

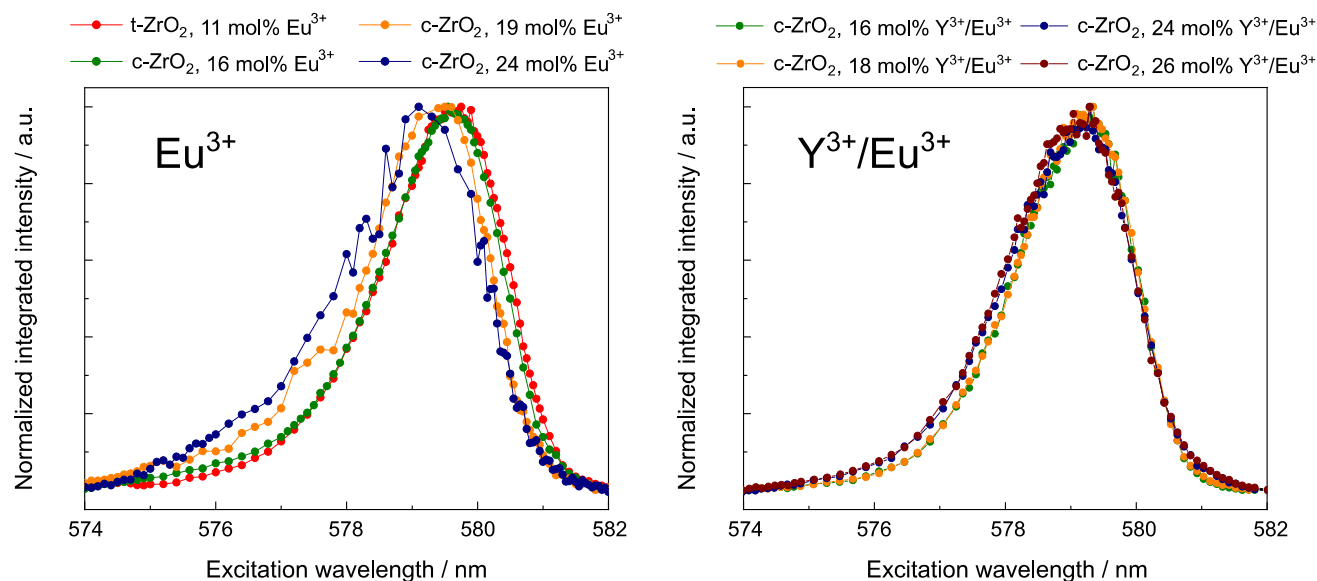


Figure 5 Selected excitation spectra of Eu^{3+} doped zirconia samples with doping fractions of 11 to 24 mol% (left). Excitation spectra of $\text{Y}^{3+}/\text{Eu}^{3+}$ co-doped zirconia with doping fractions of 16 to 26 mol% (right).

24 mol%, respectively. A similar behavior is obtained for the $\text{Y}^{3+}/\text{Eu}^{3+}$ co-doped samples. However, the clear peak shift toward higher energies occurs for higher substitutions, i.e., for 24 and 26 mol% (Fig. 5, right). The differences between the peak positions serve as a first indication for the presence of multiple nonequivalent Eu^{3+} environments in the solid phases.

A more detailed comparison of the excitation spectra of solely Eu^{3+} doped and $\text{Y}^{3+}/\text{Eu}^{3+}$ co-doped samples can be found in SI (Figure S4).

Emission spectra High-resolution emission spectra were recorded at varying excitation wavelengths for Eu^{3+} doped and $\text{Y}^{3+}/\text{Eu}^{3+}$ co-doped zirconia solid solutions. In Fig. 6, emission spectra collected at an excitation wavelength of 579.5 nm (excitation peak maximum, see Fig. 5) for selected M^{3+} doped ZrO_2 compositions are presented.

A clear threefold splitting of the $^5\text{D}_0 \rightarrow ^7\text{F}_1$ transition can be observed for the $\text{Y}^{3+}/\text{Eu}^{3+}$ co-doped samples (Fig. 6, left). However, it should be noted that the first peak of the $^5\text{D}_0 \rightarrow ^7\text{F}_1$ transition is overlapped by defect luminescence resulting from the M^{3+} incorporation. This defect luminescence has been observed before in similar systems and will be described in detail in a following study [50, 91]. The equivalent Eu^{3+} doped samples yield a rather broad $^5\text{D}_0 \rightarrow ^7\text{F}_1$ peak, where the threefold splitting is not

as well resolved (Fig. 6, right). It is, however, clear that the expected splitting pattern for Eu^{3+} incorporation in a cubic environment, i.e., onefold and two-fold splitting of the $^7\text{F}_1$ and $^7\text{F}_2$ bands, respectively, is not obtained in any of the examined solid phases. Instead, the degeneracy is fully lifted by the surrounding ligand field, corresponding to Eu^{3+} incorporation in a low-symmetry environment. The $^7\text{F}_2$ -band shows a very peculiar splitting pattern. For low-symmetry systems, a full fivefold splitting of this band is expected. Instead, only three resolved signals can be deduced from the spectra. In addition, the $^5\text{D}_0 \rightarrow ^7\text{F}_2$ transition is different in the $\text{Y}^{3+}/\text{Eu}^{3+}$ co-doped samples than in the purely Eu^{3+} doped ones. In the Y-containing samples, the main peak is shifted from 606 nm to 607 nm and it shows a shoulder on its blue side, at 605 nm (indicated in Fig. 6, left with a blue arrow). The shoulder on the red side of the main peak of the Eu^{3+} doped samples at 611 nm (red arrow in Fig. 6, right) can, however, not be observed in the $\text{Y}^{3+}/\text{Eu}^{3+}$ co-doped samples. The origin for this difference must be related to the presence of different Eu^{3+} environments in the solid phases.

In purely Eu doped samples, highly concentrated samples will result in excitation energy transfer between adjacent Eu^{3+} species and an overall quenched luminescence signal. The excitation energy transfer hampers any distinction between nonequivalent species since the emission spectra are almost

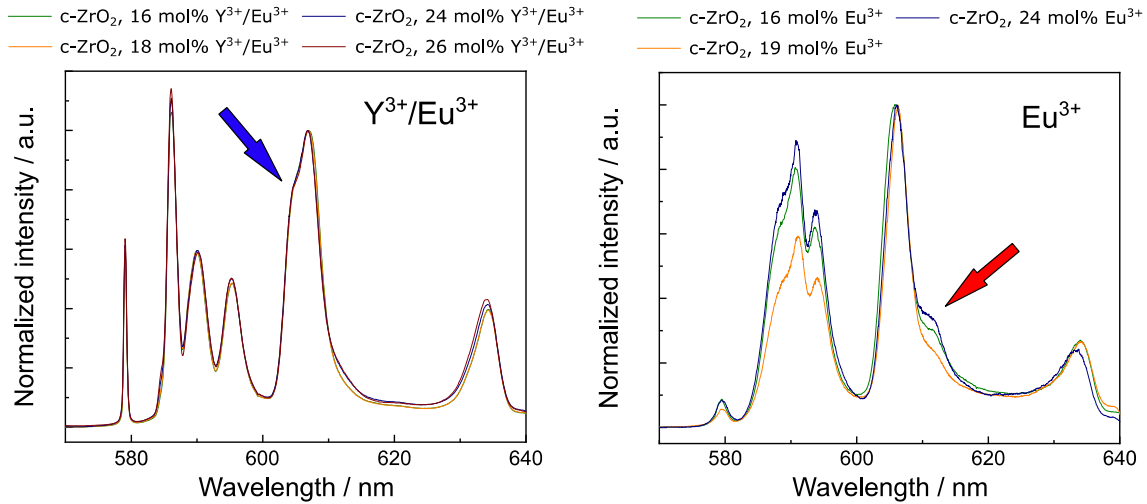


Figure 6 Emission spectra of Y^{3+}/Eu^{3+} co-doped zirconia doped with 16–26 mol% (left) and emission spectra of Eu^{3+} doped zirconia with doping percentages from 16 to 24 mol% (right), $\lambda_{ex} = 579.3$ nm, normalized to the peak maximum of the

$^5D_0 \rightarrow ^7F_2$ transition due to the presence of defect luminescence especially prominent in the Y^{3+}/Eu^{3+} co-doped samples. The arrows highlight differences in the emission spectra collected for Y^{3+}/Eu^{3+} - and Eu^{3+} doped samples.

identical, independent of the incident excitation wavelength. Thus, for further discussion of the luminescence emission behavior, only the Y^{3+}/Eu^{3+} co-doped zirconia solid solutions will be considered. Due to the low overall Eu^{3+} doping in these samples (0.5 mol%), we can assume full isolation of Eu-centers and no excitation energy transfer between nonequivalent Eu^{3+} species. Further insight into the

energy transfer effect is given in SI in relation to Figure S5.

Figure 7 shows emission spectra of an Y^{3+}/Eu^{3+} co-doped sample collected at three different excitation wavelengths. Emission spectra recorded using an excitation wavelength of 577.2 nm are clearly different from the emission recorded at 579.3 nm (Fig. 7, left). In the $^5D_0 \rightarrow ^7F_1$ transition, all three peaks are broadened in comparison with the ones

c-ZrO₂, 16 mol% Y³⁺/Eu³⁺

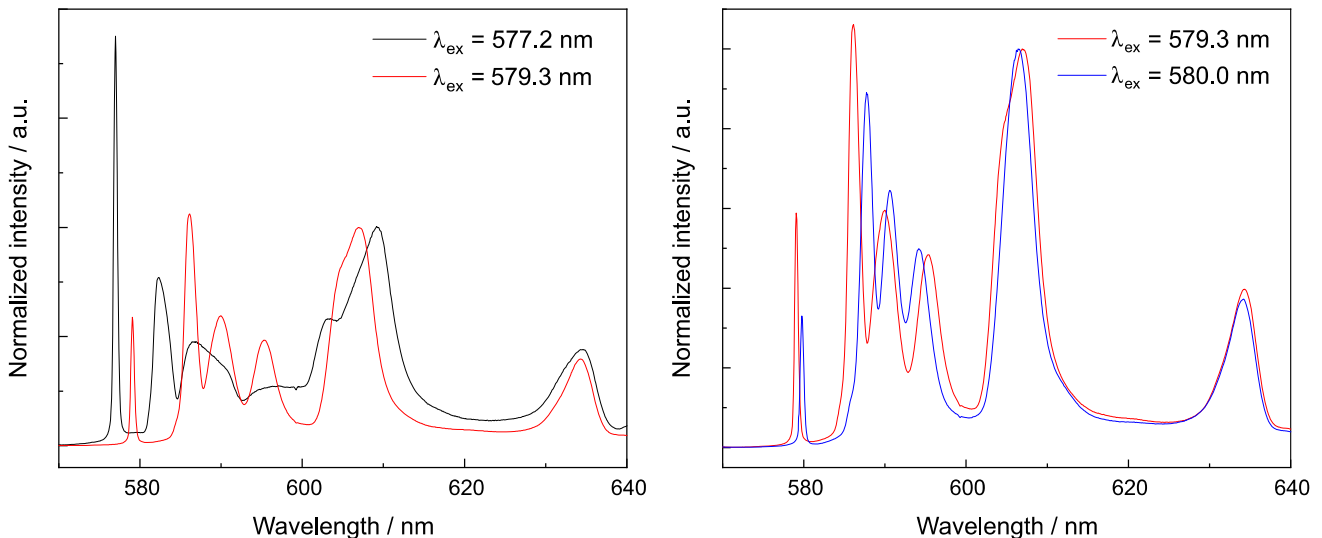


Figure 7 Comparison of emission spectra of Y^{3+}/Eu^{3+} co-doped ZrO₂ samples (16 mol% Y^{3+}/Eu^{3+}) excited at 577.2 nm versus 579.3 nm (left) and excited at 579.3 nm versus 580.0 nm (right).

from excitation at 579.3 nm; especially, the second and third peaks seem to be caused by an overlap of two unresolved peaks each. The main peak of the ${}^5D_0 \rightarrow {}^7F_2$ emission at 579.3 nm has a peak maximum at 607.0 nm with the aforementioned shoulder at about 605 nm. When exciting at 577.2 nm, the transition is split into two peaks, one at 603.1 nm and one at 609.2 nm, while the peak at 609.2 nm is also broadened on the blue side, indicating the presence of another species. Due to overlapping excitation energies of the species, emission peaks belonging to the Eu^{3+} species excited at 579.3 nm can also be deduced in the spectrum recorded at $\lambda_{\text{ex}} = 577.2$ nm. However, this rather large peak splitting in the 7F_1 as well as the 7F_2 band indicates a rather disordered Eu^{3+} environment.

When comparing the emission after excitation at 579.3 nm and 580.0 nm, rather similar spectra are obtained (Fig. 7, right), which differ from the one obtained at $\lambda_{\text{ex}} = 577.2$ nm, regarding the peak positions as well as considerably smaller peak splitting within the 7F_1 and 7F_2 bands. Interestingly, the splitting of the 7F_1 band is smaller for the Eu^{3+} environment excited at $\lambda_{\text{ex}} = 580.0$ nm than for $\lambda_{\text{ex}} = 579.3$ nm, resulting in slightly different 7F_1 band positions. For $\lambda_{\text{ex}} = 580.0$ nm, the main peak is located at 606.4 nm, compared to at 607.0 nm for 579.3 nm excitation, and it is slightly narrower, pointing toward a more ordered Eu^{3+} environment.

Lifetimes The lifetimes of the Eu^{3+} doped zirconia phases have been recorded for additional insight into the species present in the system. It can be observed that the luminescence lifetimes stay fairly constant after excitation at 579.3 nm with increasing Eu^{3+} doping until about 11 mol% (Fig. 8). A bi-exponential fit yields two lifetimes $\tau_1 = 2500 \mu\text{s}$ and $\tau_2 = 5000 \mu\text{s}$. At higher doping, a clear decrease in the lifetimes is observed. This phenomenon can be assigned to the self-quenching of Eu^{3+} . Therefore, the fitting of the lifetimes at high doping does not provide further information, and we continue the discussion of the $\text{Y}^{3+}/\text{Eu}^{3+}$ co-doped samples.

In contrast to the samples doped with Eu^{3+} only, the lifetimes of the $\text{Y}^{3+}/\text{Eu}^{3+}$ co-doped samples all yield very similar results and no self-quenching effect can be observed. All samples in the row of 16 and 26 mol% Y^{3+} doping and at all three excitation wavelengths (577.2 nm, 579.3 nm and 580.0 nm) could be fitted by using three different lifetimes, i.e.,

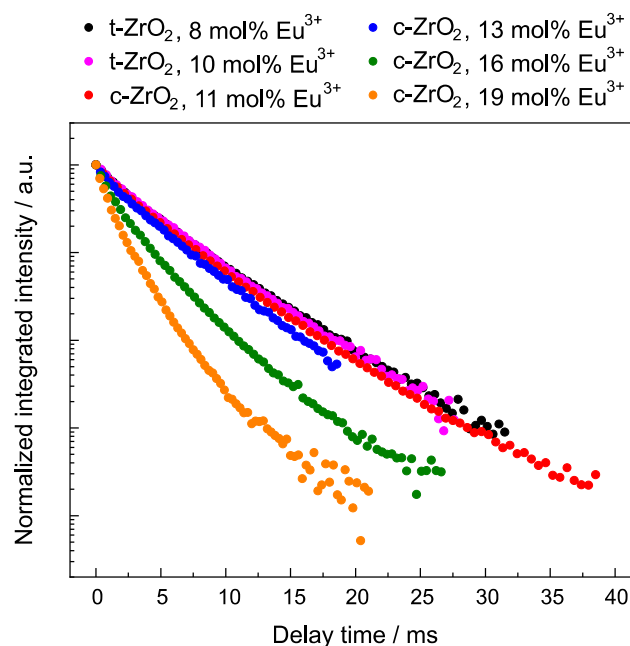


Figure 8 Luminescence lifetimes of Eu^{3+} doped zirconia with doping percentages from 8 to 19 mol% ($\lambda_{\text{ex}} = 579.3$ nm, $T \sim 10$ K).

$\tau_1 = 1030 \pm 310 \mu\text{s}$, $\tau_2 = 2950 \pm 250 \mu\text{s}$ and $\tau_3 = 6560 \pm 360 \mu\text{s}$. Examples of the decay curves and fits are presented in Figure S6. According to the Horrocks equation [Eq. (1)], the first lifetime τ_1 yields a coordination of 0.4 H_2O molecules on average, while the two longer lifetimes correlate with no water in the coordination sphere.

EXAFS and XPDF studies of the local structure of M^{3+} doped zirconia

Nearly identical background corrected and normalized absorption spectra were obtained for the four samples in the $\text{Y}^{3+}/\text{Eu}^{3+}$ co-doping row from 16 to 26 mol%. These are presented in Figure S7 for both the Y and Zr K-edge. In Fig. 9, a comparison of the resulting EXAFS (left) and their Fourier transform (right) for the Zr K-edge (top) and the Y K-edge (bottom) is presented. It can be seen that all samples in the range from 16 to 26 mol% yield a very similar EXAFS with only subtle differences.

To allow for the detection of potentially very small changes in the EXAFS spectra as a function of dopant concentration, the data reduction and the fitting (including the k -range and fixed parameters) were kept constant for all samples and for both the Zr- and Y-K edges. To find the optimal parameters, varying fitting

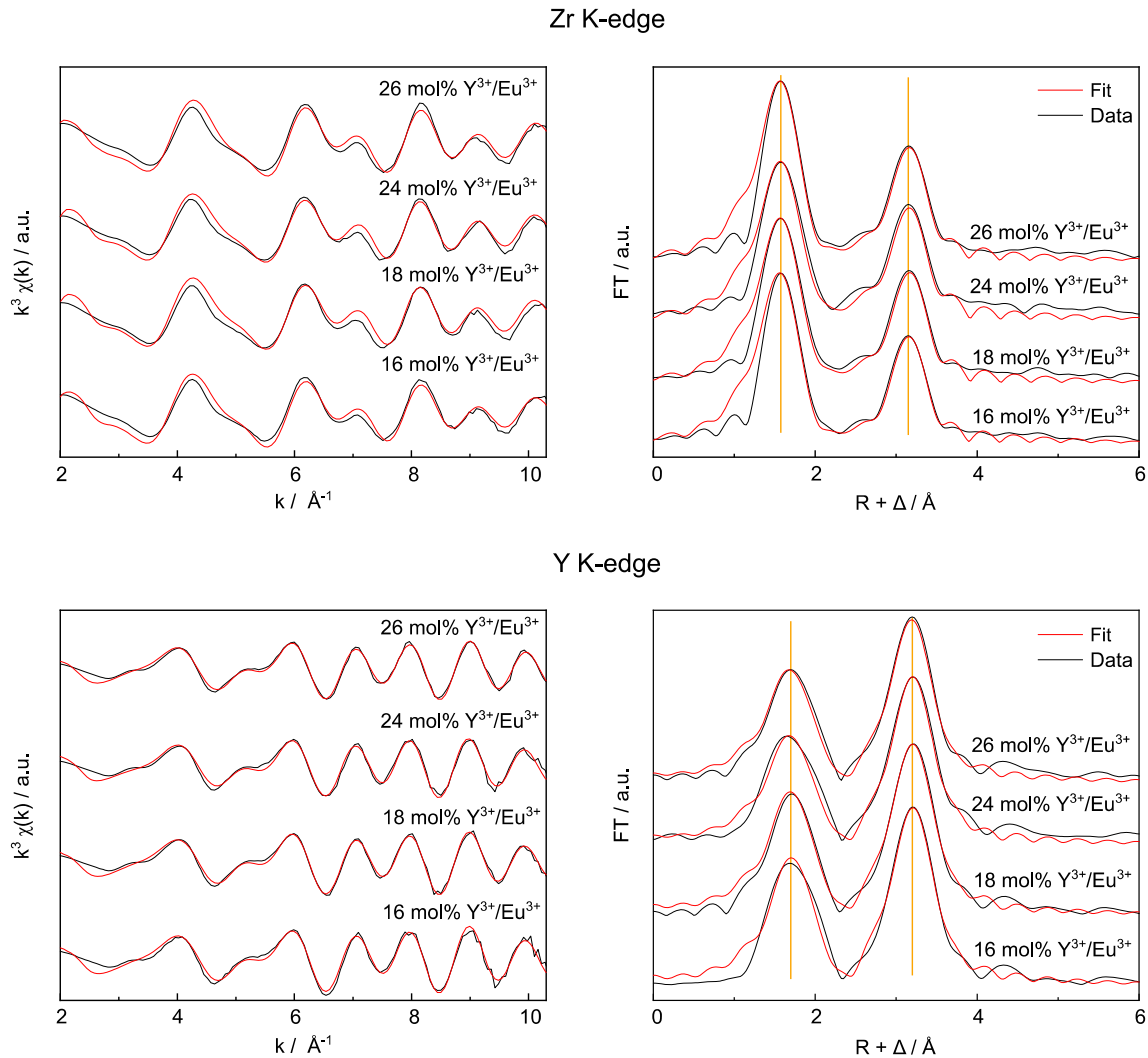


Figure 9 Experimental (black) and fitted (red) k^3 -weighted EXAFS data (left) and FT (right) of Y^{3+}/Eu^{3+} co-doped zirconia with doping levels of 16–26 mol% at the Zr K-edge (top) and Y K-edge (bottom). Orange lines are a visualization help only.

approaches were used using either fixed or fitted coordination numbers (CN). The CN fitting of the absorber–O path (abs–O) did not yield a reasonable trend (see Table S3) and was then fixed to 8. The same is true for the abs–cation (abs–M) CN, which was fixed to 12 (see Tables S4 and S5). Furthermore, the usage of a variety of shell combinations ranging from two up to five shells (see Tables S6–S8) yielded most reasonable fitting results using four shells (abs–O, abs–M, second abs–O and a multiple scattering path of abs–O–M). The results of these fits are compiled in Table 2.

Indeed, no clear trend can be derived from the obtained fit. In addition, no splitting was observed for the Zr–O shell, which is often described for the tetragonal zirconia phases [92, 93].

The obtained average Zr–O distance is very constant over the whole doping range where a slight increase from 2.14 to 2.15 Å can be observed from 16 to 24 mol%. The Zr–cation distance gives a constant value of 3.55 Å varying only within margin of error. The Y–O distance and the Y–M distance are constant within margin of error over the whole doping range with values of 2.32 Å and 3.61 Å, respectively, and therefore, larger than for the corresponding Zr shells. This translates to the shells at higher radial distance, i.e., the MS path of M–O–M as well as the second Y–O shell where also larger values are obtained in comparison with the corresponding Zr paths.

The obtained EXAFS results can be compared to the fits from the XPDF data, for which Zr–O, Eu–O and Zr–M distances are compiled in Table S2. The

Table 2 Structural parameters derived from the k^3 -weighted EXAFS spectra for the Zr and the Y K-edge

Y ³⁺ content/mol%	Path	Zr K-edge			Y K-edge		
		R/Å	CN	$\sigma^2/\text{Å}^2$	R/Å	CN	$\sigma^2/\text{Å}^2$
16	abs-O	2.141	8*	0.012	2.321	8*	0.010
	abs-M	3.550	12*	0.014	3.612	12*	0.009
	abs-O-M	3.957	48*	0.019	4.171	48*	0.008
18	abs-O	4.331	24*	0.041	4.503	24*	0.033
	abs-O	2.146	8*	0.013	2.316	8*	0.011
	abs-M	3.557	12*	0.014	3.607	12*	0.010
24	abs-O-M	3.935	48*	0.024	4.157	48*	0.005
	abs-O	4.352	24*	0.044	4.488	24*	0.036
	abs-O	2.153	8*	0.013	2.317	8*	0.012
26	abs-M	3.556	12*	0.013	3.605	12*	0.010
	abs-O-M	3.873	48*	0.027	4.144	48*	0.012
	abs-O	4.382	24*	0.048	4.476	24*	0.044
26	abs-O	2.147	8*	0.011	2.313	8*	0.012
	abs-M	3.550	12*	0.013	3.605	12*	0.010
	abs-O-M	3.935	48*	0.026	4.144	48*	0.012
	abs-O	4.338	24*	0.049	4.476	24*	0.044

Fixed CNs are marked with an asterisk (*). Fitting range is 2–10.5 Å⁻¹, R: radial distance, error ± 0.01 Å, CN: coordination number, error ± 20%, σ^2 : Debye–Waller factor, error ± 0.001 Å², amplitude reduction factor (S_0^2) = 1.0, number of independent points = 16. The average R values of the Zr K-edge fits and the Y K-edge fits are 7.8 ± 1.1 and 6.3 ± 0.6, respectively. The average ΔE_0 is – 6.7 ± 0.6 eV for the Zr K-edge and 0.9 ± 0.6 eV for the Y K-edge

Zr–O distance obtained with XPDF is slightly shorter (2.11–2.12 Å) in comparison with the EXAFS results (2.14–2.15 Å) but the general agreement is very good. The opposite trend is seen for the Eu–O (XPDF) versus Y–O (EXAFS) distance, where the former bond length is approximately 3% longer than the latter one. This correlates very well with the difference in cation radii, which is larger by approximately 4% for Eu³⁺ in comparison with Y³⁺ [94]. In other words, due to the larger size of Eu³⁺, a larger Eu–O bond length in ZrO₂ is expected. In agreement with the EXAFS data, no clear trends in the derived bond lengths can be discerned from the XPDF data. In general, however, the abs-O and abs-M distances agree very well with existing data for Y doped ZrO₂ samples of various compositions [45, 95]. They also confirm the trend reported in multiple studies, where hardly any change in the host or dopant distances to the coordinating oxygen atoms can be deduced despite the linear increase in the unit cell parameters derived from PXRD data [45, 49]. The very constant M³⁺-to-ligand distances in all investigated compositions explain the persistent excitation peak positions observed in the luminescence spectroscopic investigations described above.

EXAFS investigations studying the different crystal phases of zirconia have shown significant differences in the spectra, despite their very similar local environments [43]. Such differences are not observed in the present study. In these samples, only one major crystal phase, the cubic phase, is present. However, based on the combined results from the recorded luminescence excitation and emission spectra as well as the luminescence lifetimes, several slightly different M³⁺ environments are expected in the ZrO₂ solid phases.

These differences are likely to be too small to be discernable with the EXAFS and XPDF methods, implying that the resulting fits shown above are averages of all species present in the samples.

Discussion

With the help of PXRD, it can be seen that the cubic zirconia phase dominates the phase composition of all samples with some remaining tetragonal zirconia in the intermediate doping range (below 25 mol%). With the combination of PXRD and XPDF, the formation of a secondary phase could be excluded. As

briefly mentioned before, the crystallites of the Eu^{3+} -doped samples are approximately three times smaller than the $\text{Y}^{3+}/\text{Eu}^{3+}$ co-doped ones for comparable dopant concentrations. This is likely an effect of the cation radius, which is larger for Eu^{3+} in comparison with Y^{3+} , resulting in a larger strain and stronger lattice distortion in the samples with a direct influence on the maximum crystallite size. This may be of importance for applications where the crystallite size directly influences the material performance, such as its optical properties [96, 97], oxygen ion conductivity [98] or dissolution rate and degradation [99–103]. Despite that our combined PXRD and XPDF analyses showed a linear increase in the lattice parameters with increasing dopant concentration, indicative of solid solution formation, several of our luminescence spectroscopic observations point toward the presence of multiple distinct dopant environments in the solid structure, i.e., Eu^{3+} sites with differing coordination environments. Arguments for this can be found in the shifting of the excitation peak at very high doping, as well as the differing emission spectra and lifetimes for differing excitation energies in the individual samples. The presence of multiple Eu^{3+} environments in stabilized ZrO_2 solids has been reported in multiple studies. Montini et al. [55] have studied $\text{Eu}^{3+}/\text{Ce}^{4+}$ co-doped zirconia phases and found clear evidence for the presence of three nonequivalent Eu^{3+} environments in the stabilized host structures based on the collected Eu^{3+} excitation spectra. The authors attributed the more redshifted species with peak positions of 579.5 nm and 580.5 nm to two nonequivalent incorporation species due to the presence of different sites in the solid matrix. A blueshifted component with a peak position around 578.5 nm was shown to arise from Eu^{3+} incorporation into a superficial site. In studies by Yugami et al. [104] and Borik et al. [51, 52], three to four different Eu^{3+} environments in $\text{Y}^{3+}/\text{Eu}^{3+}$ co-doped polycrystalline samples or single crystals of zirconia, respectively, were observed. The authors attributed the specific emission signals to the formation of oxygen vacancies in the crystal structure and the subsequent change in the oxygen coordination number around the Eu^{3+} cation depending on the location [nearest-neighbor (NN) or next-nearest-neighbor (NNN) positions] of the oxygen vacancies.

Thus, in analogy with these studies, our excitation profiles were fitted using multiple Gaussian peaks. The best fit was achieved using three Gaussian peaks

to fit the overall excitation spectra (see Fig. 10 for two examples and Figure S8 for all fits). The peak positions for the samples from 11 to 24 mol% Eu^{3+} and 16 to 26 mol% Y^{3+} doping were first fitted by varying all parameters. Thereafter, the obtained average values for the peak positions of the present species, namely 578.1 ± 0.5 nm (species 1), 579.0 ± 0.4 nm (species 2) and 579.7 ± 0.5 nm (species 3), were fixed to avoid overparametrization. All samples could be fitted with these peak positions. The results of the fitting of all excitation spectra are summarized in Table 3.

Some systematic trends can be deduced from the obtained Gaussian fits of the excitation profiles. A systematic decrease in the full width at half maximum (FWHM) can be observed from species 1 to species 3. This is in line with the recorded emission spectra at excitation wavelengths of 577.2 nm (predominantly exciting species 1), 579.3 nm (predominantly exciting species 2), and 580.0 nm (predominantly exciting species 3), where emission peak narrowing could be recorded from species 1 to species 3. In addition, the overall magnitude of the crystal field splitting of the ${}^7\text{F}_1$ band decreases in the same order pointing toward a lowering of the crystal-field perturbation. Thus, there seems to be a systematic increase in the local order in these three Eu^{3+} environments (species 1 \rightarrow species 3).

In both the Eu^{3+} doped and $\text{Y}^{3+}/\text{Eu}^{3+}$ co-doped samples, species 1 increases significantly for samples of high doping where a clear shift of the excitation peak was observed (see Fig. 5), while species 2 varies slightly in the range of 30–45% for Eu^{3+} doping and 51–55% for $\text{Y}^{3+}/\text{Eu}^{3+}$ co-doped samples. Species 3 decreases in both cases with increasing doping fraction to about 10% for the highest doping fractions used here.

The obtained peak position for species 1 of 578.1 nm agrees rather well with the peak position of 578.5 nm obtained by Montini et al. [55] for Eu^{3+} incorporation at the zirconia surface. In the zirconia single crystals studied by Borik et al. [51, 52], such a blueshifted ${}^7\text{F}_0$ peak position was not observed. However, given the much smaller surface area of a single crystal compared to nanoparticle powder, no significant contribution of a surface-associated Eu^{3+} species to the luminescence is expected. The increasing trend of species 1 with increasing doping percentage follows the trend of decreasing crystallite size seen in the PXRD bulk studies (see Table 1). This is visualized in Figure S9. Thus, it is likely that the

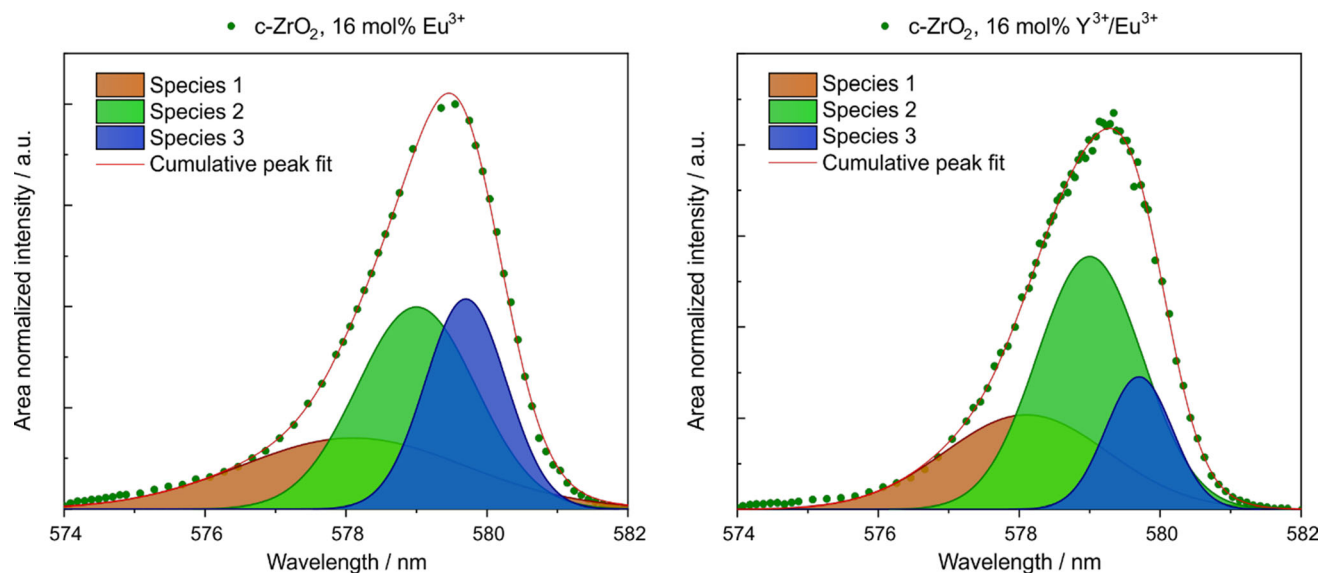


Figure 10 Gaussian fits of excitation spectrum collected for 16 mol% Eu^{3+} doped (left) and $\text{Y}^{3+}/\text{Eu}^{3+}$ co-doped $c\text{-ZrO}_2$ (right).

Table 3 Summary of the fitting results from the Gaussian fitting of the excitation spectra from TRLFS

M^{3+} doping/mol%	Species 1			Species 2			Species 3		
	λ_c/nm	%	FWHM/nm	λ_c/nm	%	FWHM/nm	λ_c/nm	%	FWHM/nm
Eu^{3+}									
11	578.1*	22	2.47	579.0*	37	1.84	579.7*	41	1.31
13	578.1*	24	2.91	579.0*	46	1.75	579.7*	30	1.20
16	578.1*	28	3.19	579.0*	42	1.69	579.7*	30	1.15
19	578.1*	48	3.00	579.0*	35	1.26	579.7*	17	0.94
24	578.1*	58	2.83	579.0*	30	1.31	579.7*	12	1.00
Y^{3+}									
16	578.1*	30	2.31	579.0*	52	1.49	579.7*	18	0.95
18	578.1*	31	2.29	579.0*	51	1.45	579.7*	18	0.99
24	578.1*	38	2.65	579.0*	51	1.57	579.7*	11	0.92
26	578.1*	37	2.67	579.0*	55	1.58	579.7*	8	0.88

Fixed values are marked with an asterisk (*)

Eu^{3+} dopant is located on a superficial site, which will increase in abundance as the crystallite size decreases. This hypothesis is further supported by the larger abundance of this species 1 in the Eu^{3+} doped ZrO_2 solid phases, which are smaller in crystallite size, in comparison to the $\text{Y}^{3+}/\text{Eu}^{3+}$ co-doped ones, which yield larger crystallites. Due to lattice relaxations at a superficial site, a higher degree of freedom and therefore a greater variety of coordination spheres are possible, resulting in the rather large FWHM in comparison with the two other species.

The excitation peak positions of species 2 (579.0 nm) and species 3 (579.7 nm) are very similar to those identified by Borik et al. [52] at 578.9 nm and 579.3 nm for $\text{Y}^{3+}/\text{Eu}^{3+}$ co-doped ZrO_2 . Excitation spectra with similar excitation peak positions can also be deduced from the data in Yugami et al.; however, exact peak positions for the extracted species were not given. In Borik et al., the abundance of the latter species was seen to increase with increasing doping, leading to the conclusion that the species results from a Eu^{3+} environment with one oxygen vacancy in the first coordination sphere. Due to a subsequent

decreasing trend of the excitation peak at 578.9 nm, this Eu^{3+} environment was assigned to an eightfold coordinated Eu^{3+} site with oxygen vacancies located only at NNN positions. Exactly the opposite trend was reported in Yugami et al. for the investigated polycrystalline $\text{Y}^{3+}/\text{Eu}^{3+}$ co-doped samples. Based on their data, the excitation peak at > 579 nm, decreasing in abundance with increasing dopant concentration, was attributed to the pristine Eu^{3+} environment, coordinating to eight oxygen atoms in the crystal structure. Based on our results presented in Table 3, a trend similar to what was observed in Yugami et al. can be deduced for species 3, where an increasing dopant substitution in the ZrO_2 solid phases results in a decrease in its fraction. The percentage of this species is very similar in both the Eu^{3+} and $\text{Y}^{3+}/\text{Eu}^{3+}$ co-doped sample compositions, i.e., the amount of this species seems to be related to the overall dopant concentration. In order to visualize the trends of the various Eu^{3+} species derived in the present study, the mole percentages of all Eu^{3+} species and the number of oxygen vacancies have been plotted as a function of the $\text{Y}^{3+}/\text{Eu}^{3+}$ co-doping in Fig. 11, left, and $\text{Eu}^{3+} + \text{Y}^{3+}$ doping fractions in Fig. 11, right.

A line for the distribution of oxygen vacancies around the Eu^{3+} ion (orange line), assuming a random (nonpreferential) distribution of the vacancies in

the crystal lattice, has been included in the figures. For more details of these plots, the reader is referred to the SI (Equations S1–S3 and Figure S10). In both the pure Eu^{3+} doping row and the $\text{Y}^{3+}/\text{Eu}^{3+}$ co-doping row, species 2 can be seen to correlate well with the overall number of oxygen vacancies; especially, in the $\text{Y}^{3+}/\text{Eu}^{3+}$ samples (Fig. 11, right), the amount of this species and the number of oxygen vacancies are almost identical. In the case of solely Eu^{3+} doped ZrO_2 (Fig. 11, left), an increase in the amount of species 2 from 11 to 16 mol% doping can be seen, after which a plateau is obtained. In this plateau region, a strong increase in the surface-associated species (species 1) occurs, which may explain the lower amount of species 2 in these Eu^{3+} doped samples in comparison with the $\text{Y}^{3+}/\text{Eu}^{3+}$ co-doped ones. In general, however, this species clearly follows the trend of the increasing amount of oxygen vacancies in the host lattice with increasing M^{3+} doping, which implies that this Eu^{3+} environment is associated with an oxygen vacancy in the first coordination sphere, i.e., in NN position.

Species 3 on the other hand is rather low in abundance over the whole investigated dopant concentration range, and the overall amount of the species is rather constant or slightly declining. As no correlation between the number of oxygen vacancies and species 3 can be seen, it is not reasonable to assume

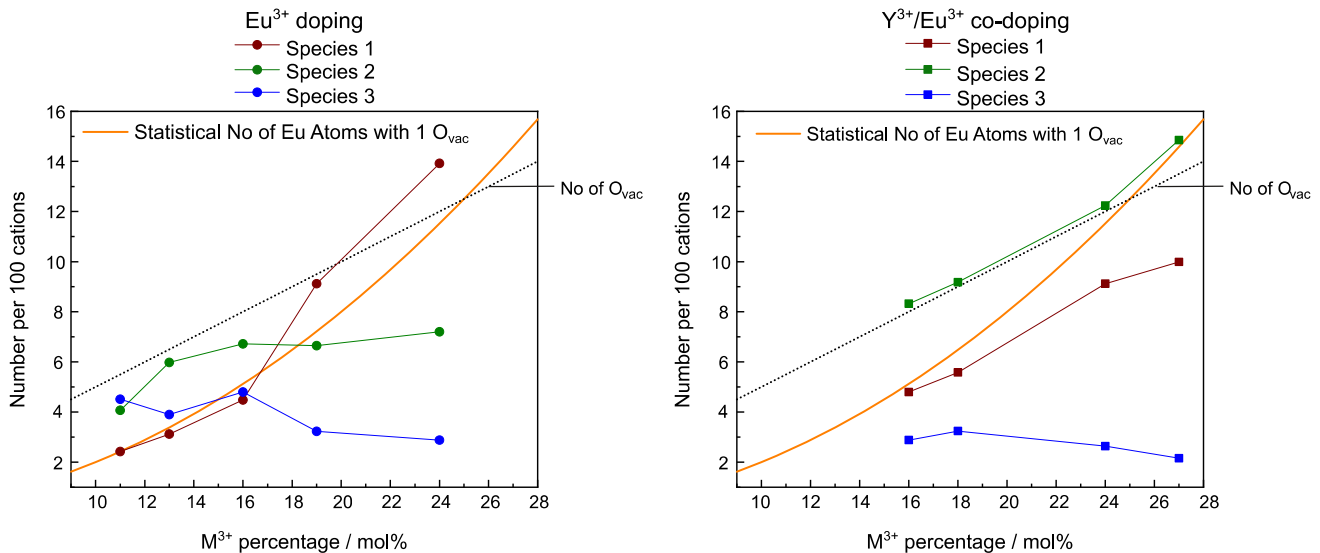


Figure 11 Number of oxygen vacancies in dependence of the Eu^{3+} doping fraction (black, dotted line) and number of cations with an oxygen vacancy in the first coordination sphere of Eu (orange line), assuming a nonpreferential, statistical distribution.

Number of species 1 (purple), species 2 (green) and species 3 (blue) Eu cations in the pure Eu^{3+} doping row (dots, left) as well as the $\text{Y}^{3+}/\text{Eu}^{3+}$ co-doped row (squares, right) per 100 cations.

that this species is Eu^{3+} associated with one oxygen vacancy in the crystal structure as found in Borik et al. [52] but rather a Eu^{3+} species surrounded by eight oxygen atoms in the crystal lattice, in agreement with the assignment in Yugami et al. [104]. Reasons for these contradicting observations could be the very different sample types used in the different studies. While Borik et al. used single crystals of Eu^{3+} doped YSZ in their luminescence spectroscopic investigations, polycrystalline powder samples have been used in the current study and in the study by Yugami et al. These are not in thermodynamic equilibrium due to the slow cation mobility in these phases. Another reason for the dissimilar results could be the different excitation wavelengths used to excite the Eu^{3+} species. In Borik et al., excitation was performed via the ${}^5\text{D}_1 \leftarrow {}^7\text{F}_0$ transition with a constant wavelength of 532 nm. In Yugami et al. and the present work, site-selective ${}^5\text{D}_0 \leftarrow {}^7\text{F}_0$ excitation spectra were collected by varying the excitation wavelength. This way, different crystal field perturbations of the various Eu^{3+} environments are taken into account, i.e., preferential excitation of a species with a matching energy gap (energy of incident laser light versus energy of the ${}^5\text{D}_1 \leftarrow {}^7\text{F}_0$ or ${}^5\text{D}_0 \leftarrow {}^7\text{F}_0$ transition) does not take place.

Interestingly, for dopant percentages of 11–16 mol% (Eu^{3+} doped samples) and of 13–26 mol% ($\text{Y}^{3+}/\text{Eu}^{3+}$ co-doped samples), the amount of Eu^{3+} species with the oxygen vacancy in NN position (species 2) is larger than the statistical distribution of vacancies between Zr and Eu. This implies that oxygen vacancies have a slight tendency for the dopant Eu^{3+} in our samples. Even though both Yugami et al. and Borik et al. reported on the relative amounts of Eu^{3+} species with one or two vacancies in NN or NNN positions in their ZrO_2 host phases, our study is the first one to report on the preferential location of oxygen vacancies for Eu^{3+} doped ZrO_2 samples. Therefore, a direct comparison with other experimental studies using Eu^{3+} as dopant cation cannot be made. There are nonetheless both experimental [105] and computational [58] studies supporting the results obtained in the present study, where a preferential location of oxygen vacancies in the crystal lattice has been found in the direct coordination of other oversized trivalent dopants rather than Zr^{4+} . These studies, however, are outnumbered by both experimental results and computational evidence for the preferential location

of oxygen vacancies around Zr^{4+} . This vacancy formation around the Zr host is explained to promote the stabilization of the tetragonal and cubic zirconia phases at ambient conditions as the reduction of the Zr–O coordination from eight to seven reduces the stress around the rather small host cation. We therefore have reason to believe that the sample synthesis procedure in terms of calcination time and temperature has a strong influence on the location of oxygen vacancies in the crystal lattice. As already discussed in connection to the phase composition of our synthetic zirconia samples, our samples are not in thermodynamic equilibrium due to the very slow cation diffusion in ZrO_2 at 1000 °C, which, however, is a rather typical calcination temperature in the synthesis of ZrO_2 [1, 26, 106, 107]. Although the anion mobility in stabilized zirconia is higher, the same assumption can be applied for the oxygen distribution in the crystal lattice. When the dopant is introduced into the zirconia solid phase, vacancy formation occurs next to the dopant due to the charge mismatch ($\text{M}^{3+} \leftrightarrow \text{M}^{4+}$) [58]. For short synthesis times, especially when combined with rather moderate temperatures, oxygen migration through the lattice may not reach a steady state which subsequently results in an unexpected distribution of oxygen vacancies in the crystal lattice. Thus, we assume that an increase in the calcination time and calcination temperature would drive the vacancies toward the host cations.

Finally, having assigned the three Eu^{3+} environments in the ZrO_2 crystal structures, an attempt was made to designate the measured luminescence lifetimes to these Eu^{3+} species. To do so, an excitation spectrum of $\text{Y}^{3+}/\text{Eu}^{3+}$ co-doped ZrO_2 with an overall dopant concentration of 18 mol% was measured after a delay time of 8 ms and compared to the excitation spectrum recorded 1 μs after the laser pulse (Figure S11). Based on the recorded lifetimes of $\tau_1 = 1030 \pm 310$, $\tau_2 = 2950 \pm 250$ and $\tau_3 = 6560 \pm 360 \mu\text{s}$, the excitation spectrum after a delay of 8 ms should show no presence of the species with the shortest lifetime and approximately 7% and 30% of the species with lifetimes of 2950 μs and 6560 μs , respectively. However, as evident from Figure S11, only a shoulder on the blue side, corresponding to species 1, is completely absent from the delayed excitation spectrum, while the main peak has remained rather unchanged. Based on this, the short lifetime of $1030 \pm 310 \mu\text{s}$ can indeed be assigned to

the surface-associated Eu^{3+} species. This lifetime is rather short for a fully incorporated Eu^{3+} ion. In fact, the *Horrocks* equation [Eq. (1)] would predict partial hydration of Eu^{3+} with on average 0.4 H_2O molecules coordinating to the cation. Species 2 and species 3, on the other hand, seem to have rather similar lifetimes based on the very constant excitation peak shape independent of delay. This is likely to be related to some energy transfer mechanism either from Eu^{3+} to Eu^{3+} centers or, more likely, between Eu^{3+} centers and defect electrons present in the lattice, which hampers the assignment of individual Eu^{3+} environments in the crystal structure based on their luminescence decay properties.

Our EXAFS investigations of ZrO_2 -doped samples with dopant concentrations ranging from 16 to 26 mol% show almost identical Zr–O/Zr-cation or Y–O/Y-cation distances of $2.147 \pm 0.005/3.553 \pm 0.004 \text{ \AA}$ and $2.317 \pm 0.003/3.607 \pm 0.003 \text{ \AA}$, respectively, over the entire compositional range. Furthermore, from EXAFS as well as XPDF, it can be excluded that the first Zr–O shell is split into 2×4 subshells in these samples. It is striking that despite a rather large difference in the Zr–O and Y–O distance ($\sim 8\%$), the Zr-cation and Y-cation distances are very similar (difference of $\sim 1.5\%$). The changes introduced by the oversized dopant are therefore mostly limited to the first coordination sphere. This observation was explained by Li et al. [43] with the deformability of oxygen ligands as well as with the continuum elasticity theory, where a quadratic decay of the radial displacement is predicted.

Nevertheless, the different species observed with TRLFS cannot be observed with EXAFS as both the Zr and Y environments stay constant over a large doping range. As EXAFS yields information of the average Zr or Y environment in the sample, the distinction of nonequivalent species in complex samples such as the investigated M^{3+} doped ZrO_2 ones is hardly possible. In our sample rows, multiple structural changes take place simultaneously. With increasing doping, oxygen vacancies are formed in the lattice, decreasing the overall M–O CN. However, at the same time, the crystallite size decreases with increasing doping leading to a higher abundance of superficial sites. The changes in the fractions of the three species observed with TRLFS are rather small, further hindering the observation of a trend in the EXAFS fits; especially, the structural difference between species 2 and 3 is vastly defined by a change

in the M–O coordination number. However, the determination of the coordination number with EXAFS inhibits a rather larger error and the coordination number in ZrO_2 does not seem to be captured properly by EXAFS fitting. This can be seen in our attempts to fit the coordination numbers (see Table S3), as well as in the literature, where the coordination number of doped ZrO_2 is typically fixed to a certain value.

The three different species observed in our studies consist of a subset of a large multitude of slightly differing coordination environments themselves. This becomes apparent when considering that in a $3 \times 3 \times 3$ supercell of ZrO_2 doped with 16 mol% Y^{3+} , a number of $9.3 \cdot 10^{23}$ possible theoretical constellations of Zr^{4+} and Y^{3+} cations, O^{2-} anions and oxygen vacancies exist. Such multiple, similar species can lead to destructive interference of the EXAFS signal of the individual Eu^{3+} environments, causing a cancelation of their signal. Therefore, the differences of the samples observed with TRLFS are not accessible with our EXAFS investigations.

The PDF analysis based on X-ray diffraction data is not affected by self-quenching effects. Nevertheless, similar atomic distances are derived for the M–O and M–M distances and no clear trend of the atomic distances with changing doping fractions can be derived. This supports the assumption that the small changes in the system resulting from multiple species cannot be readily resolved. A self-quenching effect in the EXAFS studies could, nevertheless, be present, which could explain the differing values obtained for the second M–O distances with EXAFS and XPDF. The large number of oxygen atoms in this shell could make the self-quenching of parts of the signal rather likely. These distances, however, also inherit a rather large error margin due to the high degeneracy and a strong overlap of PDFs at this distance.

An alternative explanation for the observed differences in the luminescence behavior of the individual species, but not in the structural studies with EXAFS and XPDF could be that all three species do in fact have very similar abs-O or abs-Zr distances and that solely the change in the coordination number and the local symmetry is responsible for the differences observed in the luminescence spectroscopic investigations.

Conclusions

In the present study, we have combined bulk structural investigations with spectroscopic studies of Eu^{3+} - or $\text{Y}^{3+}/\text{Eu}^{3+}$ co-doped tetragonal and cubic zirconia polymorphs. Our bulk structural characterizations show that the dopant is homogeneously distributed in the ZrO_2 host structure, thereby stabilizing the tetragonal and cubic polymorphs with little to no changes in the phase composition when using Y^{3+} versus Eu^{3+} in the stabilization process. The incorporation of Y^{3+} and/or Eu^{3+} results predominantly in the cubic phase at doping percentages of 16 mol% and above with fractions of the tetragonal phase present until approximately 19 mol%.

Our EXAFS and XPDF results imply that even though the abs-O distances for the host (Zr) and dopant (Y or Eu) differ by about 8% or 11%, the overall average coordination environment seems to remain unchanged over the studied doping range. Further insights from luminescence spectroscopic studies, i.e., site-selective luminescence spectroscopic investigations of Eu^{3+} at temperatures below 10 K, reveal the presence of nonequivalent Eu^{3+} environments in the ZrO_2 solid structures. These Eu^{3+} environments are assumed to arise from Eu^{3+} incorporation at a superficial site (species 1, $\lambda_{\text{ex}} = 578.1$ nm) and incorporation on two bulk sites (species 2, $\lambda_{\text{ex}} = 579.0$ nm and species 3, $\lambda_{\text{ex}} = 579.7$ nm) differing in the location of the oxygen vacancies with respect to the dopant cation.

The results from our study clearly show that structural modifications, such as the phase transformation from *t*- ZrO_2 to *c*- ZrO_2 which can be described with the help of various ideal crystal structures on the bulk level, do not accurately capture the structural changes and/or displacements occurring around the incorporated dopant. A mechanistic description of such local changes requires spectroscopic techniques such as TRLSFS capable of distinguishing species or environments with very subtle differences for an adequate understanding of how bulk structural changes in terms of crystallite size or oxygen vacancy formation influence the local coordination environment of an incorporated cation. With the TRLSFS method, we could show that the applied synthesis procedure results in a preferential placement of oxygen vacancies in the direct coordination

environment of the Eu^{3+} dopant (species 2). The location of vacancies in the crystal lattice has been shown to have direct implications for the oxygen mobility in stabilized ZrO_2 and will play a role in applications such as SOFCs, where a high oxygen mobility is a prerequisite. Further, our combined bulk structural and luminescence spectroscopic results showed that the decreasing crystallite size renders Eu^{3+} at superficial sites in the zirconia matrix. The association of the dopant surface could have direct implications for the corrosion resistance and performance of crystalline zirconia ceramics used for the immobilization of actinides from nuclear fuel-related waste streams.

This study shows the importance of combining the strength of multiple techniques to understand complex systems like the solid solutions of zirconia and thereby enable an advanced understanding of the changes taking place in the material on the molecular level.

Acknowledgements

Open Access funding provided by Projekt DEAL. The authors thank Diamond Light Source for rapid access to beamline I15-1 which contributed to the results presented here. The KIT Institute for Beam Physics and Technology (IBPT) is acknowledged for the operation of the storage ring, the Karlsruhe Research Accelerator (KARA) and provision of beamtime at the KIT synchrotron source. The authors would like to thank Kathy Dardenne for assistance and discussions in relation to measurements at the INE-Beamline. Furthermore, we would like to thank Dr. Atsushi Ikeda for assistance with PXRD measurements as well as Heath Bagshaw for the great support regarding TEM sample preparation and measurements.

Funding

This work was supported by the graduate academy of the *Technische Universität Dresden* from funds of the “Exzellenzinitiative” of the German state and federal states. Sam Shaw acknowledges the STFC EnvRad-Net2 network (ST/K001787/1) which supported his involvement with this work.

Compliance with ethical standards

Conflict of interest The authors declare that they have no conflict of interest.

Electronic supplementary material: The online version of this article (<https://doi.org/10.1007/s10853-020-04768-3>) contains supplementary material, which is available to authorized users.

Open Access This article is licensed under a Creative Commons Attribution 4.0 International License, which permits use, sharing, adaptation, distribution and reproduction in any medium or format, as long as you give appropriate credit to the original author(s) and the source, provide a link to the Creative Commons licence, and indicate if changes were made. The images or other third party material in this article are included in the article's Creative Commons licence, unless indicated otherwise in a credit line to the material. If material is not included in the article's Creative Commons licence and your intended use is not permitted by statutory regulation or exceeds the permitted use, you will need to obtain permission directly from the copyright holder. To view a copy of this licence, visit <http://creativecommons.org/licenses/by/4.0/>.

Electronic supplementary material: The online version of this article (<https://doi.org/10.1007/s10853-020-04768-3>) contains supplementary material, which is available to authorized users.

References

- [1] Marin R, Sponchia G, Zucchetta E, Riello P, Enrichi F, De Portu G, Benedetti A (2013) Monitoring the $t \rightarrow m$ martensitic phase transformation by photoluminescence emission in Eu^{3+} -doped zirconia powders. *J Am Ceram Soc* 96:2628–2635. <https://doi.org/10.1111/jace.12363>
- [2] Li P, Chen IW (1994) Effect of dopants on zirconia stabilization—an X-ray absorption study: II, tetravalent dopants. *J Am Ceram Soc* 77:1281–1288. <https://doi.org/10.1111/j.1151-2916.1994.tb05403.x>
- [3] Li P, Chen IW (1994) Effect of dopants on zirconia stabilization—an X-ray absorption study: III, charge-compensation dopants. *J Am Ceram Soc* 77:1289–1295. <https://doi.org/10.1111/j.1151-2916.1994.tb05404.x>
- [4] Li P, Chen IW (1994) Effect of dopants on zirconia stabilization—an X-ray absorption study: I, trivalent dopants. *J Am Ceram Soc* 77:118–128. <https://doi.org/10.1111/j.1151-2916.1994.tb06964.x>
- [5] Ho S-M (1982) On the structural chemistry of zirconium oxide. *Mater Sci Eng* 54:23–29. [https://doi.org/10.1016/0255-5416\(82\)90026-X](https://doi.org/10.1016/0255-5416(82)90026-X)
- [6] Kašpar J, Fornasiero P, Graziani M (1999) Use of CeO_2 -based oxides in the three-way catalysis. *Catal Today* 50:285–298. [https://doi.org/10.1016/S0920-5861\(98\)00510-0](https://doi.org/10.1016/S0920-5861(98)00510-0)
- [7] Tsoga A, Gupta A, Naoumidis A, Nikolopoulos P (2000) Gadolinium-doped ceria and yttria stabilized zirconia interfaces: regarding their application for SOFC technology. *Acta Mater* 48:4709–4714. [https://doi.org/10.1016/S1359-6454\(00\)00261-5](https://doi.org/10.1016/S1359-6454(00)00261-5)
- [8] Kim J (2001) Characterization of LSM-YSZ composite electrode by ac impedance spectroscopy. *Solid State Ion* 143:379–389. [https://doi.org/10.1016/S0167-2738\(01\)00877-3](https://doi.org/10.1016/S0167-2738(01)00877-3)
- [9] Jørgensen MJ, Mogensen M (2001) Impedance of solid oxide fuel cell LSM/YSZ composite cathodes. *J Electrochem Soc* 148:A433–A442. <https://doi.org/10.1149/1.1360203>
- [10] Primdahl S (1997) Oxidation of hydrogen on Ni/Yttria-stabilized zirconia cermet anodes. *J Electrochem Soc* 144:3409–3419. <https://doi.org/10.1149/1.1838026>
- [11] de Souza S (1997) Reduced-temperature solid oxide fuel cell based on YSZ thin-film electrolyte. *J Electrochem Soc* 144:L35–L37. <https://doi.org/10.1149/1.1837484>
- [12] Koide H (2000) Properties of Ni/YSZ cermet as anode for SOFC. *Solid State Ion* 132:253–260. [https://doi.org/10.1016/S0167-2738\(00\)00652-4](https://doi.org/10.1016/S0167-2738(00)00652-4)
- [13] Lu G, Miura N, Yamazoe N (1996) High-temperature hydrogen sensor based on stabilized zirconia and a metal oxide electrode. *Sens Actuators B Chem* 35:130–135. [https://doi.org/10.1016/S0925-4005\(97\)80042-1](https://doi.org/10.1016/S0925-4005(97)80042-1)
- [14] Swain MV, Garvie RC, Hannink RHJ (1983) Influence of thermal decomposition on the mechanical properties of magnesia-stabilized cubic zirconia. *J Am Ceram Soc* 66:358–362. <https://doi.org/10.1111/j.1151-2916.1983.tb10049.x>
- [15] Rühle M, Heuer AH (1984) Phase transformations in ZrO_2 -containing ceramics II, the martensitic reaction in $t\text{-ZrO}_2$. In: Science and technology of zirconia II. American Ceramic Society, Columbus, OH, vol 12, pp 14–32
- [16] Dauskarat RH, Marshall DB, Ritchie RO (1990) Cyclic fatigue-crack propagation in magnesia-partially-stabilized zirconia ceramics. *J Am Ceram Soc* 73:893–903. <https://doi.org/10.1111/j.1151-2916.1990.tb05132.x>

- [17] Furuta S, Matsushashi H, Arata K (2006) Biodiesel fuel production with solid amorphous-zirconia catalysis in fixed bed reactor. *Biomass Bioenergy* 30:870–873. <https://doi.org/10.1016/j.biombioe.2005.10.010>
- [18] Smits K, Grigorjeva L, Millers D, Sarakovskis A, Opalinska A, Fidelus JD, Łojkowski W (2010) Europium doped zirconia luminescence. *Opt Mater* 32:827–831. <https://doi.org/10.1016/j.optmat.2010.03.002>
- [19] Smits K, Sarakovskis A, Grigorjeva L, Millers D, Grabis J (2014) The Role of Nb in intensity increase of Er ion upconversion luminescence in zirconia. *J Appl Phys* 115:213520. <https://doi.org/10.1063/1.4882262>
- [20] Smits K, Jankovica D, Sarakovskis A, Millers D (2013) Up-conversion luminescence dependence on structure in zirconia nanocrystals. *Opt Mater* 35:462–466. <https://doi.org/10.1016/j.optmat.2012.09.038>
- [21] Speghini A, Bettinelli M, Riello P, Bucella S, Benedetti A (2005) Preparation, structural characterization, and luminescence properties of Eu^{3+} -doped nanocrystalline ZrO_2 . *J Mater Res* 20:2780–2791. <https://doi.org/10.1557/JMR.2005.0358>
- [22] Reisfeld R, Saraidarov T, Pietraszkiewicz M, Lis S (2001) Luminescence of Europium(III) compounds in zirconia xerogels. *Chem Phys Lett* 349:266–270. [https://doi.org/10.1016/S0009-2614\(01\)01215-5](https://doi.org/10.1016/S0009-2614(01)01215-5)
- [23] Reisfeld R, Zelner M, Patra A (2000) Fluorescence study of zirconia films doped by Eu^{3+} , Tb^{3+} and Sm^{3+} and their comparison with silica films. *J Alloys Compd* 300–301:147–151. [https://doi.org/10.1016/S0925-8388\(99\)00714-8](https://doi.org/10.1016/S0925-8388(99)00714-8)
- [24] Gómez LA, de Menezes LS, de Araújo CB, Gonçalves RR, Ribeiro SJL, Messaddeq Y (2010) Upconversion luminescence in Er^{3+} doped and $\text{Er}^{3+}/\text{Yb}^{3+}$ codoped zirconia and hafnia nanocrystals excited at 980 nm. *J Appl Phys* 107:113508. <https://doi.org/10.1063/1.3428478>
- [25] Fidelus JD, Yatsunencko S, Godlewski M, Paszkowicz W, Werner-Malento E, Łojkowski W (2009) Relation between structural properties of Pr^{3+} -doped yttria-stabilized zirconia nanopowders and their luminescence efficiency. *Scr Mater* 61:415–418. <https://doi.org/10.1016/j.scriptamat.2009.04.034>
- [26] Huangqing L, Lingling W, Shuguang C, Bingsuo Z, Zhiwei P (2007) Effect of annealing temperature on luminescence of Eu^{3+} ions doped nanocrystal zirconia. *Appl Surf Sci* 253:3872–3876. <https://doi.org/10.1016/j.apsusc.2006.08.009>
- [27] Lai L-J, Su C-S (2000) Luminescence excitation and near edge X-ray absorption spectra of Er_2O_3 dopant on zirconia ceramics. *Mater Chem Phys* 62:148–152. [https://doi.org/10.1016/S0254-0584\(99\)00172-8](https://doi.org/10.1016/S0254-0584(99)00172-8)
- [28] Gutzov S, Assmus W (2000) The luminescence of holmium doped cubic yttria-stabilized zirconia. *J Mater Sci Lett* 19:275–277. <https://doi.org/10.1023/A:1006785908816>
- [29] Ehrhart G, Bouazaoui M, Capoen B, Ferreiro V, Mahiou R, Robbe O, Turrell S (2007) Effects of rare-earth concentration and heat-treatment on the structural and luminescence properties of europium-doped zirconia sol–gel planar waveguides. *Opt Mater* 29:1723–1730. <https://doi.org/10.1016/j.optmat.2006.09.006>
- [30] Yugami H (1990) Site-selective spectroscopy of Eu^{3+} in YSZ and Y^{3+} -doped CeO_2 . *Solid State Ion* 40–41:316–319. [https://doi.org/10.1016/0167-2738\(90\)90349-V](https://doi.org/10.1016/0167-2738(90)90349-V)
- [31] Holliday KS, Stumpf Th (2011) Using time resolved laser fluorescence spectroscopy as an internal probe for the phase changes in zirconium oxide. In: Warwick P (ed) *Environmental radiochemical analysis IV*. The Royal Society of Chemistry, London, pp 30–39. <https://doi.org/10.1039/9781849732949-00030>
- [32] Dexpert-Ghys J, Faucher M, Caro P (1984) Site selective spectroscopy and structural analysis of yttria-doped zirconias. *J Solid State Chem* 54:179–192. [https://doi.org/10.1016/0022-4596\(84\)90145-2](https://doi.org/10.1016/0022-4596(84)90145-2)
- [33] Vicente FSD, Castro ACD, Souza MFD, Li MS (2002) Luminescence and structure of Er^{3+} DOPED ZIRCONIA films deposited by electron beam evaporation. *Thin Solid Films*. [https://doi.org/10.1016/S0040-6090\(02\)00784-8](https://doi.org/10.1016/S0040-6090(02)00784-8)
- [34] Menvie Bekale V, Legros C, Haut C, Sattonnay G, Huntz A (2006) Processing and microstructure characterization of ceria-doped yttria-stabilized zirconia powder and ceramics. *Solid State Ion* 177:3339–3347. <https://doi.org/10.1016/j.ssi.2006.10.004>
- [35] Zamoryanskaya MV, Burakov BE (2000) Feasibility limits in using cerium as a surrogate for plutonium incorporation in zircon, zirconia and pyrochlore. *MRS Proc* 663:301–306. <https://doi.org/10.1557/PROC-663-301>
- [36] Walter M, Nästren C, Somers J, Jardin R, Denecke MA, Brendebach B (2007) Local atomic structure of a zirconia-based americium transmutation fuel. *J Solid State Chem* 180:3130–3135. <https://doi.org/10.1016/j.jssc.2007.08.008>
- [37] Raison PE, Haire RG, Assefa Z (2002) Fundamental aspects of am and cm in zirconia-based materials: investigations using X-ray diffraction and Raman spectroscopy. *J Nucl Sci Technol* 39:725–728. <https://doi.org/10.1080/00223131.2002.10875569>
- [38] Degueldre C, Hellwig C (2003) Study of a zirconia based inert matrix fuel under irradiation. *J Nucl Mater* 320:96–105. [https://doi.org/10.1016/S0022-3115\(03\)00175-2](https://doi.org/10.1016/S0022-3115(03)00175-2)

- [39] Pöml P, Konings RJM, Somers J, Wiss T, de Haas GJLM, Klaassen FC (2012) 3.09—Inert Matrix Fuel. In: Konings RJM (ed) Comprehensive nuclear materials. Elsevier, Oxford, pp 237–256. <https://doi.org/10.1016/b978-0-08-056033-5.00057-4>
- [40] Kulkarni NK, Sampath S, Venugopal V (2001) Studies on stabilised zirconia as host phase for the fixation of actinides, rare-earths and sodium. *Ceram Int* 27:839–846. [https://doi.org/10.1016/S0272-8842\(01\)00038-4](https://doi.org/10.1016/S0272-8842(01)00038-4)
- [41] Walter M, Somers J, Bouëxière D, Rothe J (2011) Local structure in solid solutions of stabilised zirconia with actinide dioxides (UO_2 , NpO_2). *J Solid State Chem* 184:911–914. <https://doi.org/10.1016/j.jssc.2011.02.014>
- [42] Eibl M, Virtanen S, Pischel F, Bok F, Lönnrot S, Shaw S, Huittinen N (2019) A spectroscopic study of trivalent cation (Ce^{3+} and Eu^{3+}) sorption on monoclinic zirconia (ZrO_2). *Appl Surf Sci* 487:1316–1328. <https://doi.org/10.1016/j.apsusc.2019.05.012>
- [43] Li P, Chen IW, Penner-Hahn JE (1993) X-ray-absorption studies of zirconia polymorphs. I. characteristic local structures. *Phys Rev B* 48:10063–10073. <https://doi.org/10.1103/PhysRevB.48.10063>
- [44] Degueldre C, Conradson S (2001) Characterization of ternary and quaternary zirconias by XRD and EXAFS: result comparison and data modeling. *Appl Phys A* 73:489–494. <https://doi.org/10.1007/s003390100798>
- [45] Li P, Chen IW, Penner-Hahn JE (1993) X-ray-absorption studies of zirconia polymorphs. II. Effect of Y_2O_3 dopant on ZrO_2 structure. *Phys Rev B* 48:10074–10081. <https://doi.org/10.1103/PhysRevB.48.10074>
- [46] Catlow CRA (1986) EXAFS study of yttria-stabilized zirconia. *J Am Ceram Soc* 69:272–277. <https://doi.org/10.1111/j.1151-2916.1986.tb07425.x>
- [47] Jiménez-Solís C, Esquivias L, Prieto C (1995) Short-range order of yttria doped zirconia powders study by X-ray absorption (I). *J Alloys Compd* 228:188–194. [https://doi.org/10.1016/0925-8388\(95\)01883-2](https://doi.org/10.1016/0925-8388(95)01883-2)
- [48] Esquivias L, Barrera-Solano C, Piñero M, Prieto C (1996) Short-range order of yttria doped zirconia powders studied by X-ray absorption (II). *J Alloys Compd* 239:71–76. [https://doi.org/10.1016/0925-8388\(96\)02267-0](https://doi.org/10.1016/0925-8388(96)02267-0)
- [49] Veal BW, McKale AG, Paulikas AP, Rothman SJ, Nowicki LJ (1988) EXAFS study of yttria stabilized cubic zirconia. *Physica B* 150:234–240. [https://doi.org/10.1016/0378-4363\(88\)90127-1](https://doi.org/10.1016/0378-4363(88)90127-1)
- [50] Holliday K, Finkeldei S, Neumeier S, Walther C, Bosbach D, Stumpf T (2013) TRILFS of Eu^{3+} and Ce^{3+} doped $\text{La}_2\text{Zr}_2\text{O}_7$: a comparison of defect fluorite to pyrochlore structures. *J Nucl Mater* 433:479–485. <https://doi.org/10.1016/j.jnucmat.2012.10.028>
- [51] Borik MA, Volkova TV, Lomonova EE, Myzina VA, Ryabochkina PA, Tabachkova NYu, Chabushkin AN (2017) Spectroscopy of optical centers of Eu^{3+} ions in partially stabilized and stabilized zirconium crystals. *Opt Spectrosc* 122:580–587. <https://doi.org/10.1134/S0030400X17040087>
- [52] Borik MA, Volkova TV, Kuritsyna IE, Lomonova EE, Myzina VA, Ryabochkina PA, Tabachkova NYu (2019) Features of the local structure and transport properties of $\text{ZrO}_2\text{-Y}_2\text{O}_3\text{-Eu}_2\text{O}_3$ solid solutions. *J Alloys Compd* 770:320–326. <https://doi.org/10.1016/j.jallcom.2018.08.117>
- [53] Bugrov AN, Smyslov RYu, Zavalova AYu, Kirilenko DA, Pankin DV (2018) Phase composition and photoluminescence correlations in nanocrystalline $\text{ZrO}_2\text{:Eu}^{3+}$ phosphors synthesized under hydrothermal conditions. *Nanosyst Phys Chem Math* 9:378–388. <https://doi.org/10.17586/2220-8054-2018-9-3-378-388>
- [54] Soares MRN, Nico C, Peres M, Ferreira N, Fernandes AJS, Monteiro T, Costa FM (2011) Structural and optical properties of europium doped zirconia single crystals fibers grown by laser floating zone. *J Appl Phys* 109:013516–1–013516–5. <https://doi.org/10.1063/1.3527914>
- [55] Montini T, Speghini A, De Rogatis L, Lorenzut B, Bettinelli M, Graziani M, Fornasiero P (2009) Identification of the structural phases of $\text{Ce}_x\text{Zr}_{1-x}\text{O}_2$ by $\text{Eu}(\text{III})$ luminescence studies. *J Am Chem Soc* 131:13155–13160. <https://doi.org/10.1021/ja905158p>
- [56] Stapper G, Bernasconi M, Nicoloso N, Parrinello M (1999) *Ab Initio* study of structural and electronic properties of yttria-stabilized cubic zirconia. *Phys Rev B* 59:797–810. <https://doi.org/10.1103/PhysRevB.59.797>
- [57] Shimojo F, Okabe T, Tachibana F, Kobayashi M, Okazaki H (1992) Molecular dynamics studies of yttria stabilized zirconia. I. Structure and oxygen diffusion. *J Phys Soc Jpn* 61:2848–2857. <https://doi.org/10.1143/JPSJ.61.2848>
- [58] Zavodinsky VG (2004) The mechanism of ionic conductivity in stabilized cubic zirconia. *Phys Solid State* 46:453–457. <https://doi.org/10.1134/1.1687859>
- [59] Welberry TR, Butler BD, Thompson JG, Withers RL (1993) A 3D model for the diffuse scattering in cubic stabilized zirconias. *J Solid State Chem* 106:461–475. <https://doi.org/10.1006/jssc.1993.1306>
- [60] Ngai KL (1998) Evidence of interaction between oxygen ions from conductivity relaxation and quasielastic light scattering data of yttria-stabilized zirconia. *Philos Mag B* 77:187–195. <https://doi.org/10.1080/13642819808206392>
- [61] Dong Y, Qi L, Li J, Chen I-W (2017) A computational study of yttria-stabilized zirconia: I. Using crystal chemistry to search for the ground state on a glassy energy landscape.

- Acta Mater 127:73–84. <https://doi.org/10.1016/j.actamat.2017.01.006>
- [62] Kilo M, Argirusis C, Borchardt G, Jackson RA (2003) Oxygen diffusion in yttria stabilised zirconia—experimental results and molecular dynamics calculations. *Phys Chem Chem Phys* 5:2219–2224. <https://doi.org/10.1039/B300151M>
- [63] Khan MS, Islam MS, Bates DR (1998) Cation doping and oxygen diffusion in zirconia: a combined atomistic simulation and molecular dynamics study. *J Mater Chem* 8:2299–2307. <https://doi.org/10.1039/a803917h>
- [64] Gardner JA, Jaeger H, Su HT, Warnes WH, Haygarth JC (1988) Zirconia dynamics studied by PAC spectroscopy. *Phys BC* 150:223–229. [https://doi.org/10.1016/0378-4363\(88\)90125-8](https://doi.org/10.1016/0378-4363(88)90125-8)
- [65] Baudry A, Boyer P, de Oliveira AL (1982) ^{181}Ta Gamma-Gamma angular correlation study of oxygen self-diffusion in heavily defective oxides. *J Phys Chem Solids* 43:871–880. [https://doi.org/10.1016/0022-3697\(82\)90036-1](https://doi.org/10.1016/0022-3697(82)90036-1)
- [66] Winterer M (2000) Reverse Monte Carlo analysis of extended X-ray absorption fine structure spectra of monoclinic and amorphous zirconia. *J Appl Phys* 88:5635–5644. <https://doi.org/10.1063/1.1319167>
- [67] Winterer M, Delaplane R, McGreevy R (2002) X-ray diffraction, neutron scattering and EXAFS spectroscopy of monoclinic zirconia: analysis by Rietveld refinement and reverse monte carlo simulations. *J Appl Crystallogr* 35:434–442. <https://doi.org/10.1107/S0021889802006829>
- [68] King G, Soliz JR, Gordon WO (2018) Local structure of $\text{Zr}(\text{OH})_4$ and the effect of calcination temperature from X-ray pair distribution function analysis. *Inorg Chem* 57:2797–2803. <https://doi.org/10.1021/acs.inorgchem.7b03137>
- [69] Qiu X, Thompson JW, Billinge SJL (2004) PDFgetX2: a GUI-driven program to obtain the pair distribution function from X-ray powder diffraction data. *J Appl Crystallogr* 37:678–678. <https://doi.org/10.1107/S0021889804011744>
- [70] Farrow CL, Juhas P, Liu JW, Bryndin D, Božin ES, Bloch J, Proffen T, Billinge SJL (2007) PDFfit2 and PDFgui: computer programs for studying nanostructure in crystals. *J Phys: Condens Matter* 19:335219. <https://doi.org/10.1088/0953-8984/19/33/335219>
- [71] Wang D, Guo Y, Liang K, Tao K (1999) Crystal structure of zirconia by Rietveld refinement. *Sci China Ser Math* 42:80. <https://doi.org/10.1007/BF02872053>
- [72] Horrocks W, Sudnick DR (1979) Lanthanide ion probes of structure in biology. laser-induced luminescence decay constants provide a direct measure of the number of metal-coordinated water molecules. *J Am Chem Soc* 101:334–340. <https://doi.org/10.1021/ja00496a010>
- [73] Rothe J, Butorin S, Dardenne K, Denecke MA, Kienzler B, Löble M, Metz V, Seibert A, Steppert M, Vitova T et al (2012) The INE-beamline for actinide science at ANKA. *Rev Sci Instrum* 83:043105. <https://doi.org/10.1063/1.3700813>
- [74] Rothe J, Altmaier M, Dagan R, Dardenne K, Fellhauer D, Gaona X, Corrales EG-R, Herm M, Kvashnina KO, Metz V et al (2019) Fifteen years of radionuclide research at the KIT synchrotron source in the context of the nuclear waste disposal safety case. *Geosciences* 9:91. <https://doi.org/10.3390/geosciences9020091>
- [75] Ressler T (1998) WinXAS: a program for X-ray absorption spectroscopy data analysis under MS-windows. *J Synchrotron Radiat* 5:118–122. <https://doi.org/10.1107/S0909049597019298>
- [76] Ankudinov AL, Ravel B, Rehr JJ, Conradson SD (1998) Real-space multiple-scattering calculation and interpretation of X-ray-absorption near-edge structure. *Phys Rev B* 58:7565–7576. <https://doi.org/10.1103/PhysRevB.58.7565>
- [77] Fabrichnaya O, Aldinger F (2004) Assessment of thermodynamic parameters in the system $\text{ZrO}_2\text{--Y}_2\text{O}_3\text{--Al}_2\text{O}_3$. *Z Für Metals* 95:27–39. <https://doi.org/10.3139/146.017909>
- [78] Chevalier J, Gremillard L, Virkar AV, Clarke DR (2009) The tetragonal-monoclinic transformation in zirconia: lessons learned and future trends. *J Am Ceram Soc* 92:1901–1920. <https://doi.org/10.1111/j.1551-2916.2009.03278.x>
- [79] Scott HG (1975) Phase relationships in the zirconia–yttria system. *J Mater Sci* 10:1527–1535. <https://doi.org/10.1007/BF01031853>
- [80] Finkeldei S, Kegler Ph, Kowalski PM, Schreinemachers C, Brandt F, Bukaemskiy AA, Vinograd VL, Beridze G, Shelyug A, Navrotsky A et al (2017) Composition dependent order–disorder transition in $\text{Nd}_x\text{Zr}_{1-x}\text{O}_{2-0.5x}$ pyrochlores: a combined structural, calorimetric and ab initio modeling study. *Acta Mater* 125:166–176. <https://doi.org/10.1016/j.actamat.2016.11.059>
- [81] Andrievskaya ER, Lopato LM (1995) Influence of composition on the T → M transformation in the systems $\text{ZrO}_2\text{--Ln}_2\text{O}_3$ (Ln = La, Nd, Sm, Eu). *J Mater Sci* 30:2591–2596. <https://doi.org/10.1007/BF00362139>
- [82] Subramanian MA, Aravamudan G, Subba Rao GV (1983) Oxide pyrochlores—a review. *Prog Solid State Chem* 15:55–143. [https://doi.org/10.1016/0079-6786\(83\)90001-8](https://doi.org/10.1016/0079-6786(83)90001-8)
- [83] Kim N, Grey CP (2003) ^{17}O MAS NMR study of the oxygen local environments in the anionic conductors $\text{Y}_2(\text{B}_{1-x}\text{B}'_x)_2\text{O}_7$ (B, B' = Sn, Ti, Zr). *J Solid State Chem*

- 175:110–115. [https://doi.org/10.1016/S0022-4596\(03\)00290-1](https://doi.org/10.1016/S0022-4596(03)00290-1)
- [84] Yao MH, Baird RJ, Kunz FW, Hoost TE (1997) An XRD and TEM investigation of the structure of alumina-supported ceria–zirconia. *J Catal* 166:67–74. <https://doi.org/10.1006/jcat.1997.1504>
- [85] Scherrer P (1918) Bestimmung der Größe und der Inneren Struktur von Kolloidteilchen mittels Röntgenstrahlen. *Göttinger Nachrichten Math Phys* 2:98–100. https://doi.org/10.1007/978-3-662-33915-2_7
- [86] Huittinen N, Arinicheva Y, Schmidt M, Neumeier S, Stumpf T (2016) Using Eu^{3+} as an atomic probe to investigate the local environment in LaPO_4 – GdPO_4 monazite end-members. *J Colloid Interface Sci* 483:139–145. <https://doi.org/10.1016/j.jcis.2016.08.027>
- [87] Xiao B, Schmidt M (2017) Incorporation of Europium(III) into scheelite-related host matrixes ABO_4 ($A = \text{Ca}^{2+}$, Sr^{2+} , Ba^{2+} ; $B = \text{W}^{6+}$, Mo^{6+}): role of A and B sites on the dopant site distribution and photoluminescence. *Inorg Chem* 56:14948–14959. <https://doi.org/10.1021/acs.inorgchem.7b02211>
- [88] Binnemans K (2015) Interpretation of Europium(III) spectra. *Coord Chem Rev* 295:1–45. <https://doi.org/10.1016/j.ccr.2015.02.015>
- [89] Reisfeld R, Velapoldi RA, Boehm L, Ish-Shalom M (1971) Transition probabilities of Europium in phosphate glasses. *J Phys Chem* 75:3980–3983. <https://doi.org/10.1021/j100695a012>
- [90] Lavín V, Rodríguez-Mendoza UR, Martín IR, Rodríguez VD (2003) Optical spectroscopy analysis of the Eu^{3+} ions local structure in calcium diborate glasses. *J Non-Cryst Solids* 319:200–216. [https://doi.org/10.1016/s0022-3093\(02\)01914-2](https://doi.org/10.1016/s0022-3093(02)01914-2)
- [91] Lochhead MJ, Bray KL (1995) Rare-earth clustering and aluminum codoping in sol–gel silica: investigation using Europium(III) fluorescence spectroscopy. *Chem Mater* 7:572–577. <https://doi.org/10.1021/cm00051a019>
- [92] Lemaux S, Bensaddik A, van der Eerden AMJ, Bitter JH, Koningsberger DC (2001) Understanding of enhanced oxygen storage capacity in $\text{Ce}_{0.5}\text{Zr}_{0.5}\text{O}_2$: the presence of an anharmonic pair distribution function in the ZrO_2 subshell as analyzed by XAFS spectroscopy. *J Phys Chem B* 105:4810–4815. <https://doi.org/10.1021/jp003111t>
- [93] Ghosh P, Priolkar KR, Patra A (2007) Understanding the local structures of Eu and Zr in Eu_2O_3 doped and coated ZrO_2 nanocrystals by EXAFS study. *J Phys Chem C* 111:571–578. <https://doi.org/10.1021/jp064722+>
- [94] Shannon RD (1976) Revised effective ionic radii and systematic studies of interatomic distances in halides and chalcogenides. *Acta Crystallogr A* 32:751–767. <https://doi.org/10.1107/S0567739476001551>
- [95] Vlaic G, Di Monte R, Fornasiero P, Fonda E, Kašpar J, Graziani M (1999) Redox property-local structure relationships in the Rh-loaded CeO_2 – ZrO_2 mixed oxides. *J Catal* 182:378–389. <https://doi.org/10.1006/jcat.1998.2335>
- [96] Ramana CV, Vemuri RS, Fernandez I, Campbell AL (2009) Size-effects on the optical properties of zirconium oxide thin films. *Appl Phys Lett* 95:231905. <https://doi.org/10.1063/1.3271697>
- [97] Amézaga-Madrid P, Hurtado-Macías A, Antúnez-Flores W, Estrada-Ortiz F, Pizá-Ruiz P, Miki-Yoshida M (2012) Synthesis, microstructural, optical and mechanical properties of yttria stabilized zirconia thin films. *J Alloys Compd* 536:S412–S417. <https://doi.org/10.1016/j.jallcom.2011.11.111>
- [98] Jiang S, Schulze WA, Amarakoon VRW, Stangle GC (1997) Electrical properties of ultrafine-grained yttria-stabilized zirconia ceramics. *J Mater Res* 12:2374–2380. <https://doi.org/10.1557/JMR.1997.0314>
- [99] Qin W, Nam C, Li H, Szpunar J (2007) Tetragonal phase stability in ZrO_2 film formed on zirconium alloys and its effects on corrosion resistance. *Acta Mater* 55:1695–1701. <https://doi.org/10.1016/j.actamat.2006.10.030>
- [100] Lange FF, Dunlop GL, Davis BI (1986) Degradation during aging of transformation-toughened ZrO_2 – Y_2O_3 materials at 250 °C. *J Am Ceram Soc* 69:237–240. <https://doi.org/10.1111/j.1151-2916.1986.tb07415.x>
- [101] Guo X (1999) On the degradation of zirconia ceramics during low-temperature annealing in water or water vapor. *J Phys Chem Solids* 60:539–546. [https://doi.org/10.1016/S0022-3697\(98\)00301-1](https://doi.org/10.1016/S0022-3697(98)00301-1)
- [102] Li J-F, Watanabe R (2005) Phase transformation in Y_2O_3 -partially-stabilized ZrO_2 polycrystals of various grain sizes during low-temperature aging in water. *J Am Ceram Soc* 81:2687–2691. <https://doi.org/10.1111/j.1151-2916.1998.tb02677.x>
- [103] Kelly J, Denry I (2008) Stabilized zirconia as a structural ceramic: an overview. *Dent Mater* 24:289–298. <https://doi.org/10.1016/j.dental.2007.05.005>
- [104] Yugami H, Koike A, Ishigame M, Suemoto T (1991) Relationship between local structures and ionic conductivity in ZrO_2 – Y_2O_3 studied by site-selective spectroscopy. *Phys Rev B* 44:9214–9222. <https://doi.org/10.1103/PhysRevB.44.9214>
- [105] Weller M (1996) Anelastic relaxation of point defects in cubic crystals. *J Phys IV* 06:C8-63–C8-72. <https://doi.org/10.1051/jp4:1996812>

- [106] Marin R, Sponchia G, Back M, Riello P (2016) Determining europium compositional fluctuations in partially stabilized zirconia nanopowders: a non-line-broadening-based method. *Acta Crystallogr Sect B Struct Sci Cryst Eng Mater* 72:29–38. <https://doi.org/10.1107/S2052520615021083>
- [107] Freris I, Riello P, Enrichi F, Cristofori D, Benedetti A (2011) Synthesis and optical properties of sub-micron sized rare earth-doped zirconia particles. *Opt Mater* 33:1745–1752. <https://doi.org/10.1016/j.optmat.2011.06.010>

Publisher's Note Springer Nature remains neutral with regard to jurisdictional claims in published maps and institutional affiliations.